

POLITECNICO DI MILANO  
Scuola di Ingegneria Industriale e dell'Informazione  
Corso di Laurea Magistrale in Ingegneria Fisica



## **Oxygen Detection Through VIPA Spectrometer**

Anno Accademico 2013-2014

Relatore: Prof.ssa Roberta Ramponi  
Dipartimento di Fisica

Correlatore: Prof.ssa Nandini Bhattacharya  
Ms. Andreas Hänsel  
Ms. Adonis Reyes Reyes  
Optics group TU Delft

Tesi di laurea di:  
Alberto Maran  
Matr. 783392

# Ringraziamenti

Per prima cosa ringrazio la Professoressa Roberta Ramponi per avermi permesso di poter svolgere la tesi all'estero, ed essere stata sempre disponibile, nonostante le distanze che ci separavano. I would like to thank Nandini, Andreas and Adonis that followed me for the whole period of my thesis, because I learnt a lot from them, and I also enjoyed working with them. I thank also the entire Optics Group, in particular Paul Urbach, for giving me the opportunity to be part of the group and make me feel like I still am part of the group. That's why now I am going to thank you all without the Optic website help, starting from Daniel, Matthiäs, Luca, Lei, Katsyarina, Nishant, Ying, Joseph, Alessandro, Roy, Mahsa, Marco, Pascal, Tim, Roland, Paul Planken, Silvana, Jeff, Peter Petrik, Peter Sommers, Edgar, Gopika, Yvonne, Aurele, Zhe, Hamhed, Nitish, Yfeng, Wouter, Gopakoumar, Alberto.

Of course I didn't forget all the hard-working master students Hugo, Jörn, George, Quincy, Sjoerd, Nick, Ton and Remo. Now I can double-check and see if I forgot someone, in that case I need to come back to Delft and offer a beer to the remaining ones.

Ringrazio ora la mia famiglia che mi è sempre stata a fianco in questo lungo percorso e non ha mai smesso di incoraggiarmi e credere in me.

I miei compagni del Poli che sono troppi, zii mi mandate in sbatta a scrivervi tutti. In ogni caso mi tocca, quindi parto da Mazzotta che ho importunato tantissime volte per problemi di svariata natura, credo manchino solo quelli idraulici all'appello. Poi Andrea che se ne è fuggito per non riparare i danni che avevamo combinato in casa, Manuz pusher di canzoni di fiducia, nonchè albergatore d'eccezione degli ultimi mesi. Sharma che insomma è pur sempre Sharma e in qualità di Sharma Boy tocca ringraziarlo perchè è l'unico milanista obiettivo sul pianeta terra. Fiiiiaaaaa siete ancora tantissimi, non ce la posso fare. Beh iniziamo con il Monti, che, se non conosci il Monti al giorno d'oggi non sei nessuno. Perchè son capaci tutti ad andare a New York a fare i selfie, ma un selfie a Lodi col Monti in quanti è che ce l'hanno? Grande Monti! Poi ci sono quei diplomatici di Gabri e Diego, mai una parola fuori posto, mai che si siano scomposti una volta davanti alle bellezze che offriva la nostra biblioteca. E i matematici, Davide, Pelle, Gaia, Diana. Voi un po' mi state antipatici (so che antipatici non rende ma è pur sempre un tesi quindi non vi ringrazio:). A parte Diana ovviamente che insomma non può stare antipatica a nessuno.

Ringrazio Chiara che mi ha sempre passato gli appunti di mille corsi e che mi ha avuto in casa per un anno intero e ha cucinato cose che non pensavo potessero essere così buone. Mi mancano i noculari, il mitico Sam compagno di bevute e cantate e il buon Dami. Ora i ragazzi dell' Atletico Prosecco con cui mi sono divertito molto a giocare e che non dimenticherò di certo.

Ringrazio anche Silvia che nel bene e nel male mi ha sempre aiutato in questo percorso e le auguro tutto il bene possibile. Adesso tocca ai vicentini, al Gab, al gruppo freccette, alla Prof. Zaltron che par sotto ha sempre dispensato consigli utili. Infine gli olandesi Marco e Fisca che sono state delle amicizie inaspettate e veramente divertenti.

## Abstract

The accuracy of long distance measurement based interferometer setups for geodetic surveying and industrial use, are impeded by the accuracy of the refraction index of air.

Temperature is the main factor influencing the refractive index as ambient fluctuations are non-uniform over the space, over time the temperature can vary by half a degree in the controlled lab environment. It is possible to obtain the temperature through spectroscopy analyzing absorption spectra changes and comparing them to HITRAN online database spectra, with an accuracy that can reach couple of degrees. The goal is having an insight on the air refractive index changes through temperature measurements of air. To do that the measurements are done on the gases composing air like CO<sub>2</sub>, O<sub>2</sub>. The spectra are revealed thanks to a VIPA spectrometer that can display the absorption suffered inside a gas cavity from a gas. The measurement consists in two step: first the gas cavity is filled with a reference gas (N<sub>2</sub>), then evacuated and filled with the gas wanted for absorption. The difference between these two measurements is then processed via software. The wavelength used for CO<sub>2</sub> measurements is 1550 nm, the wavelength for O<sub>2</sub> is 760 nm. The beams are collinear when propagating inside the cavity. The temperature measurements on CO<sub>2</sub> has already been done in the laboratory, the measurements on O<sub>2</sub> are the task of this thesis. The setup to detect O<sub>2</sub> through spectroscopy was built and, processing the data with MATLAB, the absorption spectrum was extracted. The results still need to be improve before complete temperature measurements, but are a good starting point.

## Sommario

Lo scopo finale del progetto è di poter effettuare misure interferometriche su una lunga distanza in aria, e per fare questo è importante conoscere con buona accuratezza l'indice di rifrazione dell'aria. La temperatura è il fattore principale che influenza l'indice di rifrazione dato che le fluttuazioni ambientali non sono uniformi nello spazio, mentre nel tempo la temperatura può variare di mezzo grado in un ambiente controllato. È possibile ricavare la temperatura con accuratezza che dell'ordine di pochi gradi con tecniche spettroscopiche: in particolare andando a ricavare le variazioni degli spettri di assorbimento di una molecola e comparandoli successivamente a quelli catalogati all'interno del database online di HITRAN. Lo scopo è ottenere informazioni su come cambia l'indice di rifrazione dell'aria andando ad analizzare alcuni dei gas che lo compongono come  $\text{CO}_2$  e  $\text{O}_2$ . Gli spettri di assorbimento vengono ottenuti andando a rivelare con uno spettrometro VIPA l'assorbimento che si verifica in una cavità sigillata, la quale è riempita prima con un gas di riferimento ( $\text{N}_2$ ) che non assorbe alla frequenza del laser, poi con il gas di cui si vuole ottenere lo spettro di assorbimento. Le due misure sono poi sottratte e i dati processati. Nel caso di  $\text{CO}_2$ , la lunghezza d'onda del laser utilizzato è 1550 nm, nel caso di  $\text{O}_2$  è 760 nm. I fasci sono collineari nel tratto in cui si propagano all'interno della cavità. Per quanto riguarda la  $\text{CO}_2$  sono state già condotte misure di temperatura in laboratorio, mentre le misure riguardanti  $\text{O}_2$  sono l'oggetto di questa tesi. Il setup per rivelare  $\text{O}_2$  è stato costruito e messo in funzione, acquisendo e i dati ottenuti tramite LABVIEW e processandoli grazie a MATLAB. I risultati necessitano miglioramenti, ma sono un buon punto di partenza per ottenere misure di temperatura con  $\text{O}_2$ .

## Estratto

Il lavoro svolto in questa tesi rappresenta soltanto una parte di un progetto più esteso che ha come scopo la realizzazione di misure interferometriche su lunga distanza in aria che presentino un'accuratezza tale da poter essere utilizzate in ambito industriale e per misurazioni geodetiche. Il problema principale di tali misure è dovuto all'accuratezza non ottimale con cui viene stimato l'indice di rifrazione dell'aria, che a sua volta è fortemente influenzato dalla temperatura. In particolare, la temperatura è il parametro critico su cui si concentra il nostro progetto e l'idea alla base di questo lavoro è quella di effettuare delle misure di temperatura attraverso l'analisi spettroscopica di alcuni gas che compongono l'aria, e si sono scelti  $\text{CO}_2$  e  $\text{O}_2$ .

Le misure di temperatura in questione verranno effettuate attraverso l'acquisizione degli spettri di assorbimento di  $\text{CO}_2$  e  $\text{O}_2$  e il loro confronto con i rispettivi spettri presenti nel database online di HITRAN. Questo database cataloga gli spettri di assorbimento di queste molecole al variare di alcuni parametri fisici come pressione, temperatura, numero d'onda, forma d'onda e cammino ottico. Modificando i parametri in questione è possibile interpolare i dati dello spettro ottenuto con quelli dello spettro catalogato, ricavando così il relativo valore di temperatura. Per arrivare a questo è necessario prima costruire un setup in grado di rivelare gli spettri di assorbimento di  $\text{CO}_2$  e  $\text{O}_2$ . Il setup utilizzato consiste in una cavità in cui è possibile iniettare aria,  $\text{CO}_2$ ,  $\text{O}_2$  o una miscela di entrambi. Per ottenere l'assorbimento è necessaria una sorgente laser che propaghi all'interno della cavità. Le lunghezze d'onda necessarie per avere assorbimento da parte di  $\text{CO}_2$  sono vicine a 1550 nm, quelle per  $\text{O}_2$  sono vicine a 760 nm. Si è utilizzato un Frequency Comb laser a 1550 nm per  $\text{CO}_2$ , mentre per  $\text{O}_2$  si è generata la Seconda Armonica del laser a 1550 nm utilizzando un cristallo nonlineare di Beta Borato di Bario. I cammini ottici dei due fasci sono collineari per la parte riguardante la propagazione nella cavità. La rivelazione degli spettri di assorbimento avviene tramite due spettrometri VIPA, ognuno adatto alla specifica lunghezza d'onda della sorgente laser utilizzata. Per poter ottenere dei dati sperimentali processabili, le misure di assorbimento ottico sono state effettuate in due passi successivi: il primo consiste nel riempire la cavità con il gas di cui si vuole ottenere lo spettro di assorbimento; successivamente si svuota la cavità e la si riempie con un gas di riferimento che non assorbe alla lunghezza d'onda del laser che si propaga nella cavità. Le due misure vengono poi sottratte, eliminando così contributi non imputabili al gas in esame, e sono pronte per essere processate con MATLAB utilizzando un programma che ne ricava lo spettro di assorbimento. Infine, con lo spettro di assorbimento è possibile ricavare le misure di temperatura citate all'inizio. Una volta che si ottengono misure in buon accordo con i dati catalogati su HITRAN si può passare al passo successivo, ossia modificare la temperatura della cavità osservando come variano i rispettivi spettri di assorbimento.

Nello specifico, questa tesi riguarda la costruzione e caratterizzazione del setup per rivelare lo spettro di assorbimento di  $\text{O}_2$ , lo sviluppo del software per l'acquisizione dei dati sperimentali

e il loro processamento al fine di ottenere gli spettri di assorbimento di O<sub>2</sub>. Infine sono stati analizzati e caratterizzati gli errori sperimentali presenti nelle varie misure, in modo da poter in un secondo momento migliorare il sistema per poter interpolare lo spettro acquisito con lo spettro catalogato sul database online di HITRAN.

# List of Figures

1.1.	Schematic of the experimental setup used for CO <sub>2</sub> detection and O <sub>2</sub> detection . . .	2
1.2.	Schematic guideline to illustrate the steps to perform to achieve the ultimate goal	2
2.1.	Simple sketch of the absorption process of a photon from an electron . . . . .	4
2.2.	Energy structure of a diatomic molecule [1]. The level of the electric, vibration and rotational energies are in different orders of magnitude. Two different branches originated from the change in rotation $\Delta J$ are shown . . . . .	5
2.3.	Absorption coefficient from HITRAN database assuming concentration of 100% of O <sub>2</sub> , P = 1 atm, T = 300K, the path length is not important given the fact we are simulating the absorption coefficient and not the absorption spectrum . . . . .	6
2.4.	Schematic of the setup relevant for O <sub>2</sub> absorption and detection. The branch with the gas cavity and the branch with the open air cavity are intended to be used exclusively. First the experiments with gas cavity are perform then the experiments with open air cavity. The branch with free propagation is used as reference for the open air cavity setup. . . . .	7
2.5.	Summary of the method use to obtain the absorption simulations previously described. . . . .	8
2.6.	Intensity Ratio between two measurement. The first with the gas cavity filled with air (6.5 m path length, $c = 0.2$ ), the second with N <sub>2</sub> inside the cavity (5 m path length, $c = 0.2$ ) . . . . .	8
2.7.	Absorption simulation using N <sub>2</sub> as reference and assuming the gas cavity filled with 100% O <sub>2</sub> for the measurement . . . . .	9
2.8.	Open air cavity absorption calculated using as reference part of the beam that is not passing through the cavity . . . . .	10
2.9.	Schematic of the setup relevant for O <sub>2</sub> absorption and detection with open air multipass cavity . . . . .	11
3.1.	Complete setup present on our optical table [2]. The red part regards the branch used for CO <sub>2</sub> detection, while the green part is the part about O <sub>2</sub> detection we built and characterize . . . . .	12
3.2.	Simplified setup for O <sub>2</sub> detection branch . . . . .	13
4.1.	Spectrum of a frequency comb, showing the frequency repetition rate $f_{rep}$ and the frequency offset $f_{ceo}$ . . . . .	15
4.2.	Envelope and carrier of a pulse . . . . .	15

4.3.	Frequency comb spectrum [3]	17
4.4.	Pulses train of a frequency comb [3], showing the $\Delta\phi_{CE}$	18
4.5.	Mode-locked laser frequency stabilization scheme	19
4.6.	In this picture are illustrated the processes that derive from the expansion of the second order term of the nonlinear polarization. Second Harmonic Generation, Sum Frequency Generation and Difference Frequency Generation.	22
4.7.	Schematic of the second harmonic process in a nonlinear lossless medium	22
4.8.	Normalized intensity of fundamental and second harmonic components in continuous wave, with plane wave approximation and phase matching condition $\Delta k = 0$	25
4.9.	Spectrum of second harmonic generation after BBO crystal	27
5.1.	VIPA spectrometer components [1]. The VIPA spectrometer is made of a cylindrical lens that is focusing the beam on the bottom part of the VIPA etalon, after the etalon the beam proceed towards the grating that is dispersing the spectral components in several orders and through a spherical lens is focusing onto a CMOS camera	28
5.2.	VIPA etalon. In this picture is shown the angle $\theta$ between the incident beam and the normal to the VIPA, where the virtual images are lying.	29
5.3.	VIPA etalon disperse the frequencies in different angles on the vertical line, but all of them considered separately are collimated beams	30
5.4.	Incident beam refracted inside the etalon and reflected at his rear plate	31
5.5.	Schematic of a blazed grating illustrating peculiar angles and distances [4]	33
5.6.	Main steps for rough alignment of the VIPA spectrometer [5]	38
6.1.	Example of picture out of focus at the bottom	41
6.2.	This picture is more in focus but looking carefully at the bottom it is not in focus like at the top	41
6.3.	Picture obtained with optimum settings and ambient air inside the cavity	41
6.4.	Periodic pattern of CO <sub>2</sub> obtained with the 1550 nm spectrometer by Adonis Reyes Reyes [1]	42
6.5.	Picture of the Reference diode laser with pump currents of 58 mA, 58.6 mA, 60.2 mA.	43
6.6.	Spectrum of the diode laser taken with a current intensity of 60.8 mA	44
6.7.	Beam shape of the diode laser	44
6.8.	Spectrum of the functioning reference diode laser	45
6.9.	FSR localization on the CMOS camera. The area of interest is between the red lines [6]	45
6.10.	Difference between the picture taken with O <sub>2</sub> , and the one with N <sub>2</sub> .	46
6.11.	Difference between O <sub>2</sub> picture and N <sub>2</sub> picture, after replacement of the gas cavity windows and with vacuum pump turned off [6].	47
6.12.	The spectrum at the top is the spectrum obtained with the MATLAB program, the spectrum at the bottom is the spectrum taken by HITRAN database	48



C.1. Labview program for acquisition and averaging of 25 pictures. . . . . 62

# List of Tables

- 5.1. VIPA spectrometer parameters. . . . . 37
- 5.2. VIPA alignment step using power meter. . . . . 39
  
- 6.1. Measurements done to find the noise sources . . . . . 47

# Contents

- 1. Introduction 1**
  - 1.1. Thesis Outline . . . . . 3
  
- 2. Absorption Simulations 4**
  - 2.1. Absorption Spectroscopy . . . . . 4
  - 2.2. Absorption lines . . . . . 6
  - 2.3. Simulations . . . . . 6
  - 2.4. Theoretical results . . . . . 11
  
- 3. Setup 12**
  - 3.1. Experimental Setup . . . . . 12
  
- 4. Light Source 14**
  - 4.1. Frequency Comb Laser. . . . . 14
    - 4.1.1. Frequency comb principle. . . . . 14
    - 4.1.2. Detection of the Carrier envelope offset frequency and stabilization . . . 18
  - 4.2. Second Harmonic Generation . . . . . 20
    - 4.2.1. Polarization Nonlinear effects . . . . . 20
    - 4.2.2. Second order effects . . . . . 20
    - 4.2.3. Derivation of SH field . . . . . 21
  - 4.3. Light source characterization . . . . . 27
  
- 5. VIPA Spectrometer 28**
  - 5.1. VIPA etalon . . . . . 29
  - 5.2. VIPA parameters . . . . . 31
  - 5.3. Diffraction grating . . . . . 33
  - 5.4. Numerical values of the spectrometer characteristics . . . . . 35
  - 5.5. Guideline for Alignment . . . . . 37
  
- 6. Measurements, Results and Error Analysis 40**
  - 6.1. Frequency Comb Alignment . . . . . 40
  - 6.2. FSR localization on the CMOS camera . . . . . 42
  - 6.3. Data Acquisition . . . . . 45
  - 6.4. Noise sources . . . . . 46

<b>7. Conclusions and Discussion</b>	<b>50</b>
<b>Appendices</b>	<b>53</b>
<b>A. Lambert-Beer law derivation</b>	<b>54</b>
A.1. Derivation of Lambert-Beer law . . . . .	54
<b>B. Derivation of Parabolic equation for linear propagation</b>	<b>56</b>
<b>C. Labview Program</b>	<b>61</b>

# 1. Introduction

The accuracy of long distance measurement based interferometer setups for geodetic surveying and industrial use are impeded by the accuracy of the refraction index of air. Air's refractive index is described by Edlen's equation [7] which depends on temperature, pressure, humidity and gas mixture. This equation originates from Edlen's work done in 1953 [8] Temperature is the main factor influencing the refractive index as ambient fluctuations are non-uniform over the space, over time the temperature can vary by half a degree in the controlled lab environment. This is in contrast with pressure, relative humidity and CO<sub>2</sub> and O<sub>2</sub> concentrations who are relatively uniform over the space. Furthermore these last three can be measured to a good enough precision which leaves temperature as the most uncertain influential parameter. It is possible to solve this obstacle using a large number of accurate temperature sensors (PT – 100) in order to keep track of the temperature along the path.

A different technique has been used in the chemical industry, namely measuring temperature through spectroscopy. As the absorption spectrum changes with temperature, it is possible to obtain the temperature from it by looking at how it changes. Recently this was only done for high (above 500 K) temperatures and with an accuracy of a couple of degrees. In 2010 the group of Hieta et al. [9] was able to show that measuring temperature through spectroscopy can also be done for room temperatures with an accuracy of 22 mK, which a year later they improved to 7 mK [10]. The big advantage that this brings is that the temperature measurement is done with the beam used for measurements itself, meaning that there are no restrictions regarding blocking the beam path.

The ultimate goal of the project is to have an insight on the air refractive index changes using the spectroscopic technique mentioned before.

This is going to happen through several step that will be listed here. The general idea is to build a setup that can detect absorption lines of O<sub>2</sub> and CO<sub>2</sub> using lasers of wavelengths, respectively, 760nm and 1550nm. The spectra will be used for extracting temperature measurements by comparing the spectra with the HITRAN database for different temperatures for the considered molecules.

The setup for revealing the absorption lines of CO<sub>2</sub> is already working and the achieved results are successful [1].

The part regarding O<sub>2</sub> is still in progress and my project is focused completely on the development and characterization of this setup.

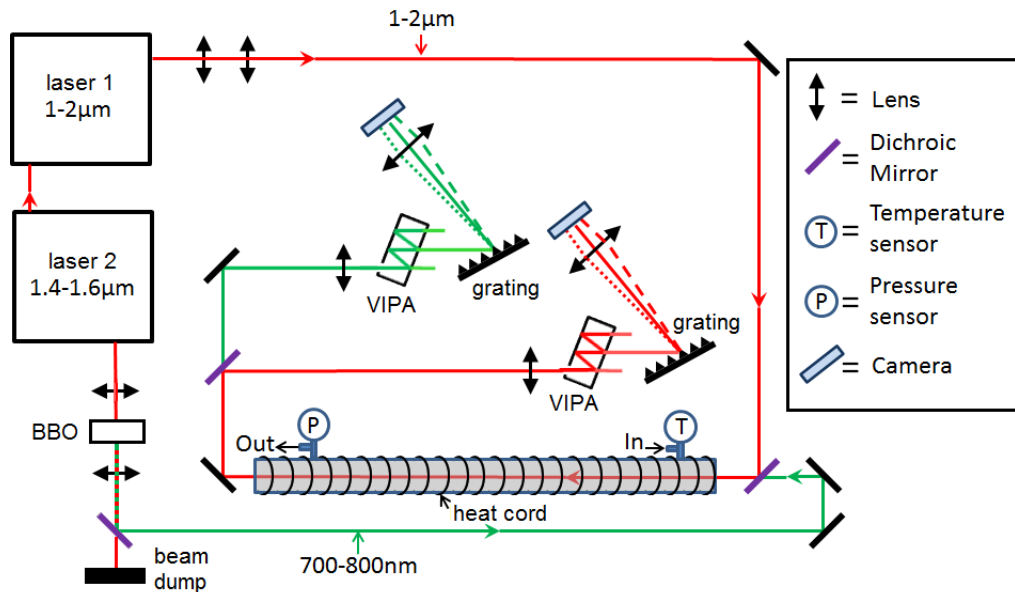


**Figure 1.1.:** Schematic of the experimental setup used for CO<sub>2</sub> detection and O<sub>2</sub> detection

More specifically a master student, Ton Verhoeven, developed the risk assessment phase for the O<sub>2</sub> detection experiment [2], I took care of building the setup, analyze and process data in order of characterize the noise level and stability of our system so that the next step can be to reveal absorption lines and compare the spectrum with the online database for the temperature measurements step.

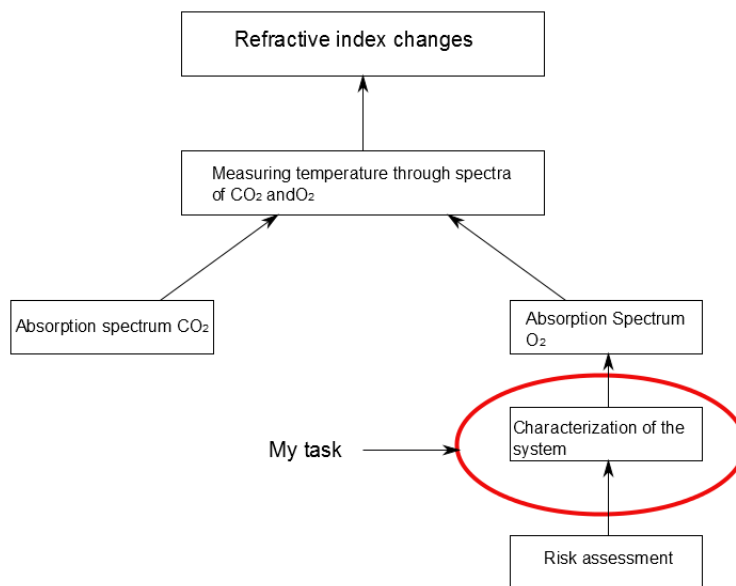


**Figure 1.2.:** Schematic guideline to illustrate the steps to perform to achieve the ultimate goal

## 1.1. Thesis Outline

This thesis is divided in three parts, the absorption simulations, the description of the setup and the detection and analysis part.

In chapter 2 the absorption lines of  $O_2$  are shown together with absorption simulations related to our setup for different concentration of  $O_2$  inside the gas cavity and for the open air cavity configuration. These measurements represent our theoretical results to later fit with our experimental results.

In chapter 3 the experimental setup is shown and later explained step by step, starting in chapter 4 from the frequency comb laser and its important parameters, as well as the technique to stabilize (Second Harmonic Generation) process where we give some theoretical insight into the process and move on to show the experimental spectrum of the SHG beam we are using as light source.

In chapter 5 we focus on the Virtually Imaged Phase Array spectrometer that allow us to detect the absorption lines of  $O_2$  and we show which are the important parameters and what their values are.

In chapter 6 all the measurements data processing are displayed and the results obtained are discussed.

## 2. Absorption Simulations

The purpose of our experiments is to reveal the absorption lines of  $O_2$  with our setup. For this purpose the original bandwidth of our frequency comb, that is 200 nm at central wavelength of 1550 nm, was not suited with the  $O_2$  absorption lines that are present in the region 759 – 762 nm. In fact a Beta Barium Borate (BBO) nonlinear crystal was used and the Second Harmonic was generated achieving a light source that fits the spectral region where it is possible to observe  $O_2$  absorption. Using the SHG beam we can detect  $O_2$  absorption if the medium where the beam is propagating contains  $O_2$ .

The setup is built in ambient air so the  $O_2$  concentration along the beam path is 20%, but a 1.5 m sealed gas cavity is present, so that filling the cavity with different  $O_2$  concentration we can achieve various configurations for the total  $O_2$  absorption. In this chapter we show three possible configurations, changing the concentration of  $O_2$  inside the cavity. The first one with the gas cavity filled with ambient air, so with a  $O_2$  concentration in the cavity of 20%, the second one with the cavity filled with 100%  $O_2$ .

The last one regards the use of an open air 1m multipass cavity, where the  $O_2$  concentration is 20% and the absorption is enhanced because the beam path is enhanced due to 20 reflections of the beam inside the cavity .

### 2.1. Absorption Spectroscopy

Absorption spectroscopy is a technique that measure the absorption of radiation due to its interaction with a sample. The sample absorbs energy and the intensity of absorption varies as a function of frequency, and this variation is the absorption spectrum. So the absorption spectrum of a molecule/element shows how much a molecule/element absorbs at a precise frequency. To measure directly the absorption of a sample the most direct technique is to send a beam of a proper frequency throughout the sample and measure the intensity of radiation before and after the sample to find out which fraction of the beam intensity passes through.

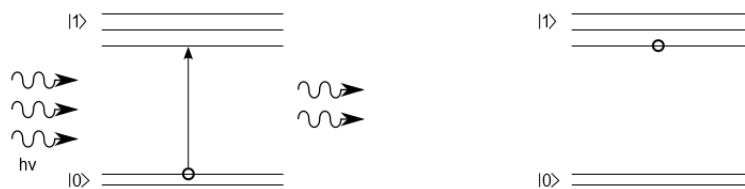


**Figure 2.1.:** Simple sketch of the absorption process of a photon from an electron



The absorption spectrum is primarily determined by the atomic and molecular composition of the material. Radiation is absorbed at frequencies that match the energy difference between two quantum mechanical states of the molecules according also to the selection rules for the transition from one quantum state to another.

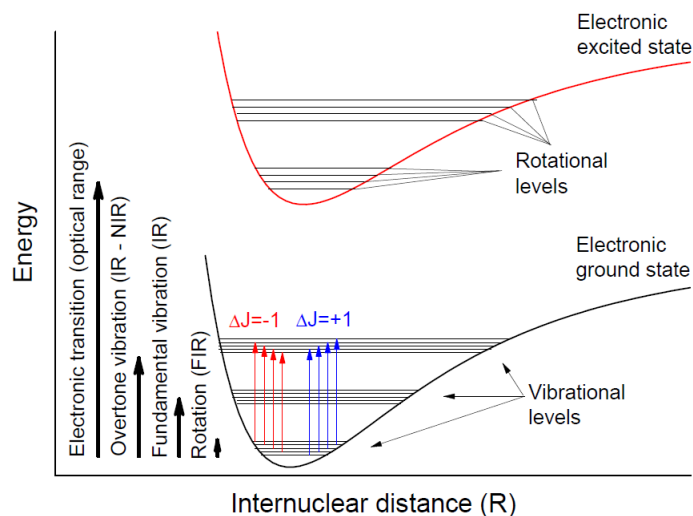


**Figure 2.2.:** Energy structure of a diatomic molecule [1]. The level of the electric, vibration and rotational energies are in different orders of magnitude. Two different branches originated from the change in rotation  $\Delta J$  are shown

In general the energy levels of a molecule are very similar to the fig 2.2, where is possible to see three different kind of energy levels. The electronic levels have band shape and bigger energy gap between them, while vibrational levels and rotational levels have lower energy gap. The usual energy gap between those levels in a transition are:

- Visible and near infrared (NIR) around  $10000 \text{ cm}^{-1}$  for electronic transitions
- NIR between  $500$  and  $1000 \text{ cm}^{-1}$  for vibrational levels
- Infrared (IR) between  $1$  and  $100 \text{ cm}^{-1}$  for rotational levels

For each kind of energy is possible to estimate a formula containing a quantum number related to the electron, the rotational and vibrational energy levels. These numbers according to quantum mechanics law follow the selection rules, so that not all the transitions are allowed [11] .

The absorption that occurs due to a transition between two states is referred to as an absorption line and a spectrum is typically composed of many lines. The frequencies where absorption lines occur, as well as their relative intensities, depend on the electronic and molecular structure of the sample, together with the selection rules. The frequencies will also depend on the interactions between molecules in the sample, and on several environmental factors (e.g., temperature, pressure, electromagnetic field). The lines will also have a width and shape that are determined by the spectral density or the density of states of the system.

In our case the absorption spectrum of  $O_2$  is well known and registered on HITRAN database online, where setting many parameters ( pressure, temperature, concentration, optical path, wavenumber, wavenumber step) is possible to obtain the absorption spectrum.

## 2.2. Absorption lines

As already mentioned accessing to HITRAN online database we obtained the absorption spectrum for  $O_2$  for a 100% concentration, atmospheric pressure, ambient temperature 300K.

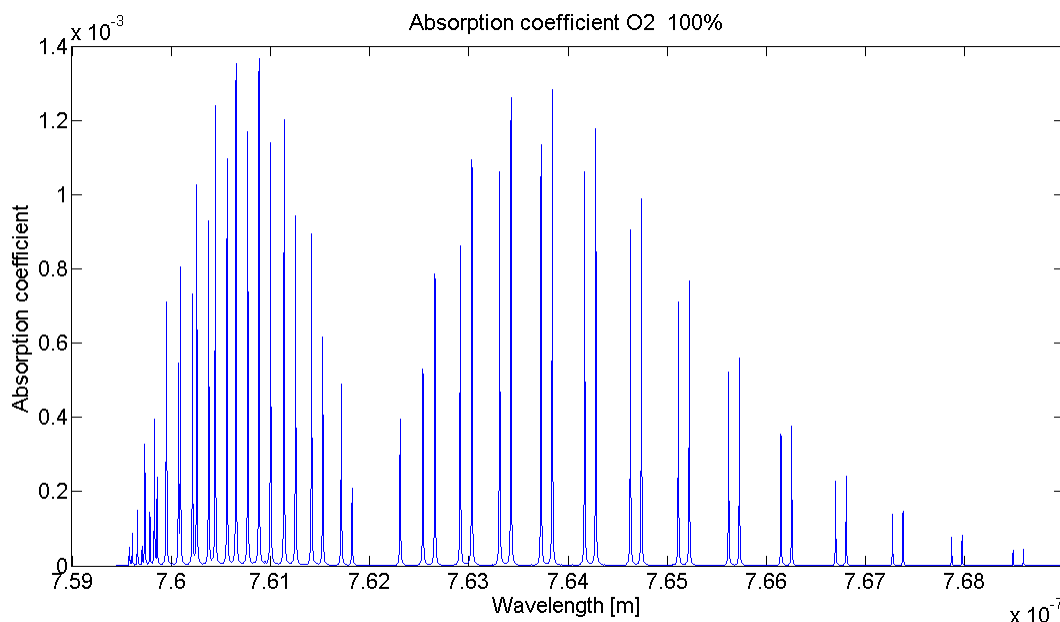


**Figure 2.3.:** Absorption coefficient from HITRAN database assuming concentration of 100% of  $O_2$ ,  $P = 1$  atm,  $T = 300K$ , the path length is not important given the fact we are simulating the absorption coefficient and not the absorption spectrum

It is possible to see that the main absorption peaks are localized around 760 nm, and later we will show that the SHG of the original laser should have enough power to allow us to reveal absorption in this region.

## 2.3. Simulations

The next step is to simulate the expected absorption for our experiment using Lambert-Beer law ( derivation in appendix A ) and using the data of  $O_2$  absorption coefficient given by HITRAN

database displayed in fig 2.3.

$$I = I_0 e^{-\alpha l} \quad \alpha = \varepsilon c \quad (2.1)$$

$$I = I_0 e^{-\varepsilon c l} \quad (2.2)$$

Here  $\varepsilon$  is the absorptivity,  $c$  the concentration of  $O_2$ ,  $l$  is the path length, and  $\alpha$  the absorption coefficient. In our case the total path length of the setup is 6.5 m and the concentration to take into account is the concentration of  $O_2$  in air,  $c = 0.2$ . In addition the absorptivity  $\varepsilon$  is equal to the absorption coefficient  $\alpha$  displayed in fig 2.3 because HITRAN was taking into account a concentration of 100%  $O_2$ , so  $c = 1$ , and  $\varepsilon = \alpha$ .

Given the small absorption, a reference measurement is needed, so a 1.5 m gas cavity was introduced in our setup to characterize the system. In this way the cavity can be filled with air for  $O_2$  absorption measurements and also with  $N_2$  that will act as reference gas, given the fact that it does not show absorption lines over wavelengths covered by the SH beam.

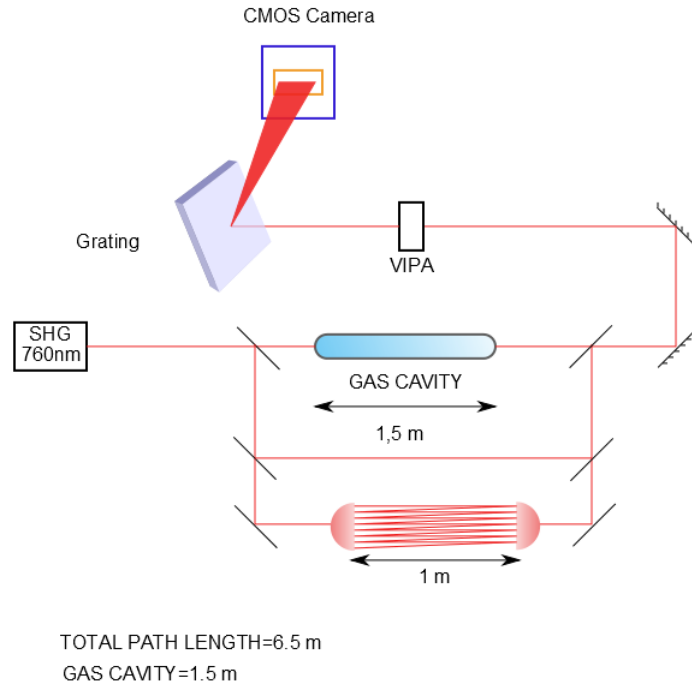


**Figure 2.4.:** Schematic of the setup relevant for  $O_2$  absorption and detection. The branch with the gas cavity and the branch with the open air cavity are intended to be used exclusively. First the experiments with gas cavity are performed then the experiments with open air cavity. The branch with free propagation is used as reference for the open air cavity setup.

Two simulations were run changing gas and concentration inside the gas cavity.

The first simulation was made taking the intensity ratio between two absorption measurements, one with  $N_2$  inside the cavity (reference gas), the other with lab air inside the cavity ( $O_2$  concentration 20%).

The total  $O_2$  absorption path for  $N_2$  measurement is just 5 m because there is no absorption inside

the cavity ( $6.5 \text{ m} - 1.5 \text{ m} = 5 \text{ m}$ ). The  $\text{O}_2$  absorption path for air is  $6.5 \text{ m}$ . In both cases the concentration of  $\text{O}_2$  is to be assumed  $20\%$ , that is the  $\text{O}_2$  concentration in air.

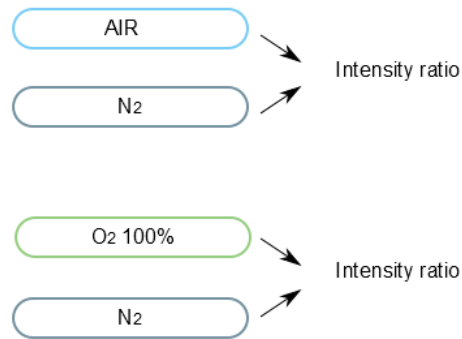


**Figure 2.5.:** Summary of the method use to obtain the absorption simulations previously described.

The first simulation regards the intensity ratio between the  $\text{O}_2$  absorption for a path length of  $6.5 \text{ m}$  in ambient air, and the  $\text{O}_2$  absorption for a shorter path ( $5 \text{ m}$ ) due to  $\text{N}_2$  inside the cavity:

$$\frac{I}{I_0} = e^{-\varepsilon c(650 \text{ cm} - 500 \text{ cm})} \quad (2.3)$$

In picture 2.6 the intensity ratio is displayed for wavelengths from  $759 \text{ nm}$  to  $769 \text{ nm}$ . The higher peak around  $760 \text{ nm}$  is showing a ratio of  $2.5\%$ .

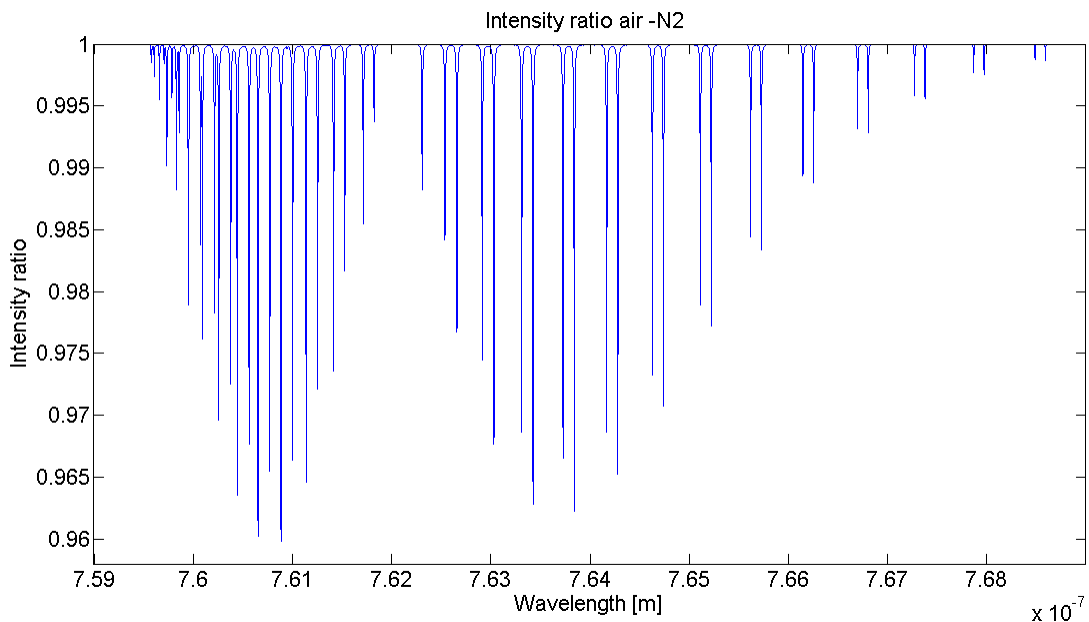


**Figure 2.6.:** Intensity Ratio between two measurement. The first with the gas cavity filled with air ( $6.5 \text{ m}$  path length,  $c = 0.2$ ), the second with  $\text{N}_2$  inside the cavity ( $5 \text{ m}$  path length,  $c = 0.2$ )

This simulation lead us to consider that a stronger absorption could be necessary in order to reveal absorption lines successfully, so another simulation considering the cavity filled with 100% O<sub>2</sub> was also run.

The second simulation considers the intensity ratio between two absorption measurements, one with N<sub>2</sub> inside the cavity (reference gas), the other with O<sub>2</sub> concentration inside the cavity of 100%. In this case the O<sub>2</sub> absorption path for the measurement with N<sub>2</sub> inside the cavity is the same as before but the O<sub>2</sub> absorption path for the measurement with 100% O<sub>2</sub> now is 0.2(500 cm) + 1(150 cm). So the intensity ratio is

$$\frac{I}{I_0} = e^{-\varepsilon[0.2(500 \text{ cm})+1(150 \text{ cm})-0.2(500 \text{ cm})]} \quad (2.4)$$

In this case the intensity ratio calculated is similar to the previous one, but the difference is focused now on the concentration of O<sub>2</sub> inside the gas cavity that is  $c = 1$ .

This change lead to an increase in absorption and the results are shown below in fig 2.7

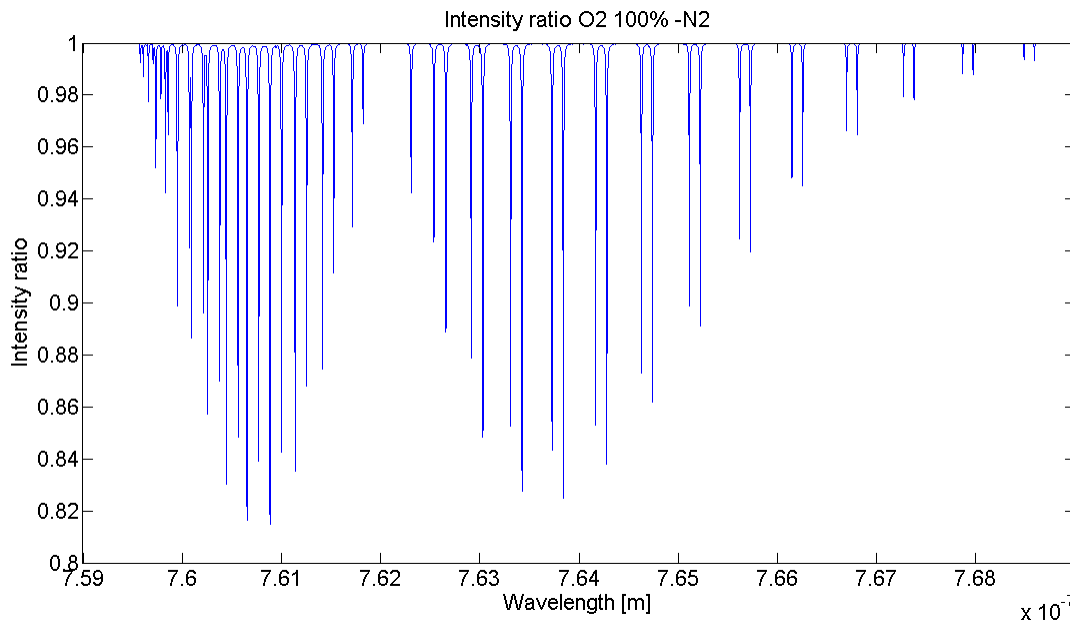


**Figure 2.7.:** Absorption simulation using N<sub>2</sub> as reference and assuming the gas cavity filled with 100% O<sub>2</sub> for the measurement

The simulations are showing absorption of 2.5%, and 12% for the two previous cases around 760 nm and the higher peaks around 761 nm are at 4%, and 18%. In order to have more absorption another idea to increase the absorption was taken into account.

The principle of this idea is to build an open air multipass cavity that should just enhance the path length of our beam providing a 20 m longer path and so a bigger absorption according to eq 2.2 and eventually allow us to detect our lines. This cavity should be one meter long and should provide the path enhancement desired due to 20 reflections inside.

In this case the concentration between two measurements is always  $c = 0.2$  and only the path is changing. Due to the fact that the open air cavity is not yet installed we do not know the total absorption path length but to calculate the intensity ratio we just need to know that the difference is 21 m, because if our cavity is going to have 20 reflections and the cavity is long one meter the total path will be 21 m and taking as reference a part of the beam that does not enter the multipass cavity the path difference will be 20 m.

$$\frac{I}{I_0} = e^{-\varepsilon[0.2(2100 \text{ cm} - 100 \text{ cm})]} \quad (2.5)$$

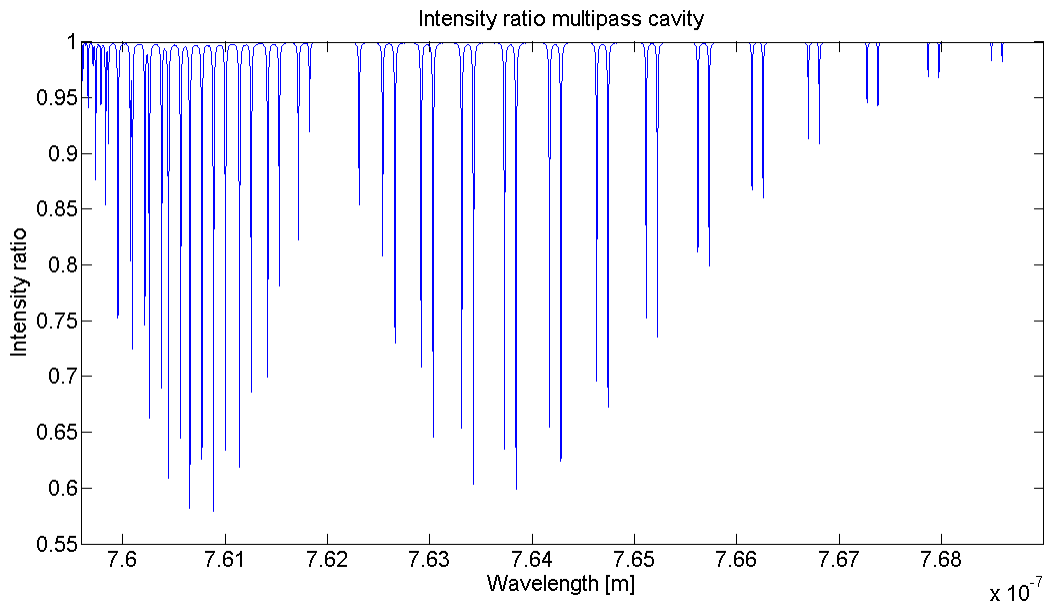


**Figure 2.8.:** Open air cavity absorption calculated using as reference part of the beam that is not passing through the cavity

In fig 2.8 the simulation for the open air cavity absorption with the path enhancement of 20 metres are shown, and in this case the absorption at 760 nm is definitely higher reaching almost 30% with a peak of 40% around 761 nm.

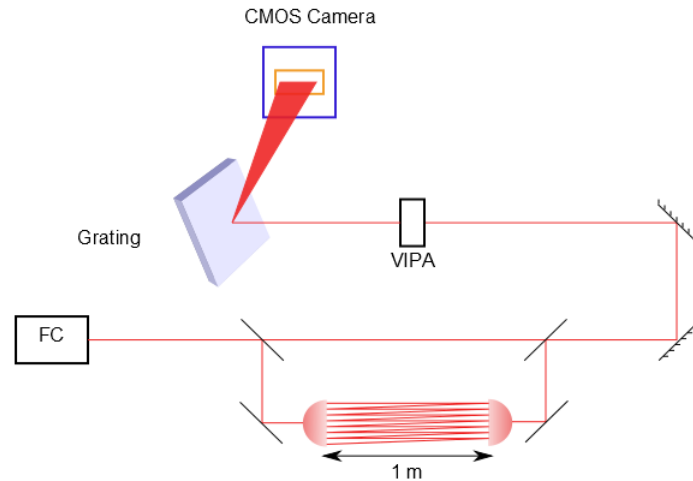


**Figure 2.9.:** Schematic of the setup relevant for  $O_2$  absorption and detection with open air multipass cavity

## 2.4. Theoretical results

This simulation shows the percentage of absorption we can obtain from  $O_2$  in three different configurations: lab air inside the cavity, 100%  $O_2$  inside the cavity, multipass cavity with 20 m path enhancement and are the first step in order to detect  $O_2$  lines with our setup. The following step is to build the setup for  $O_2$  detection, characterize its stability and noise level, obtain pictures of the experimental absorption lines and finally fit with the theoretical results.

# 3. Setup

In this chapter the experimental setup used for our project will be quickly illustrated while the precise description of the most important components (the light source and the spectrometer) will be explained in the following chapters.

## 3.1. Experimental Setup

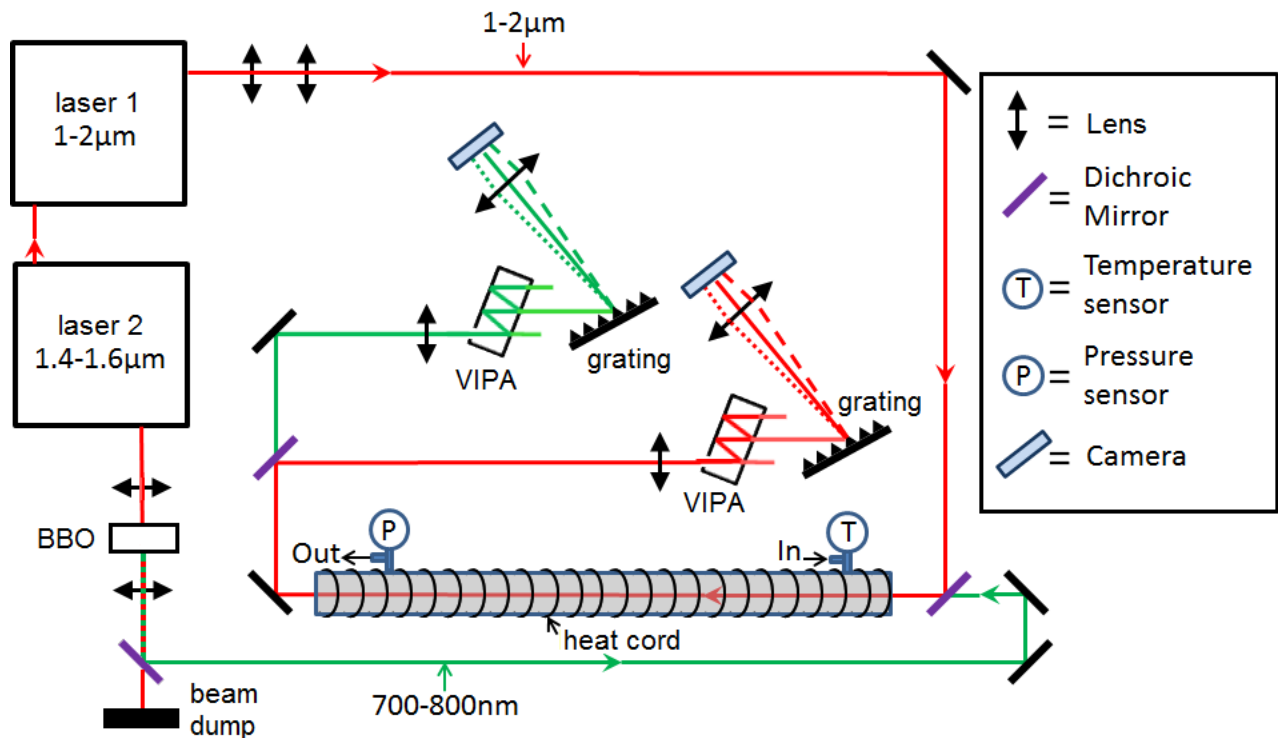


**Figure 3.1.:** Complete setup present on our optical table [2]. The red part regards the branch used for CO<sub>2</sub> detection, while the green part is the part about O<sub>2</sub> detection we built and characterize

In fig 3.1 is shown the setup used for trace detection of O<sub>2</sub> and CO<sub>2</sub> . The red branch uses the frequency comb laser at 1550 nm to detect CO<sub>2</sub> absorption lines.

This part of the setup was implemented by Adonis Reyes Reyes and the CO<sub>2</sub> lines he revealed matched with good accuracy to the theoretic ones. The green part of the setup is the section we are working on, and is used for O<sub>2</sub> trace detection. The wavelength used is the second harmonic



of the original comb and is 760 nm. Thanks to this source it is possible to detect the absorption lines of  $O_2$  using a particular spectrometer that will be discussed later. Moving on to describe better the setup we can have a look at the simplified branch for  $O_2$  trace detection.

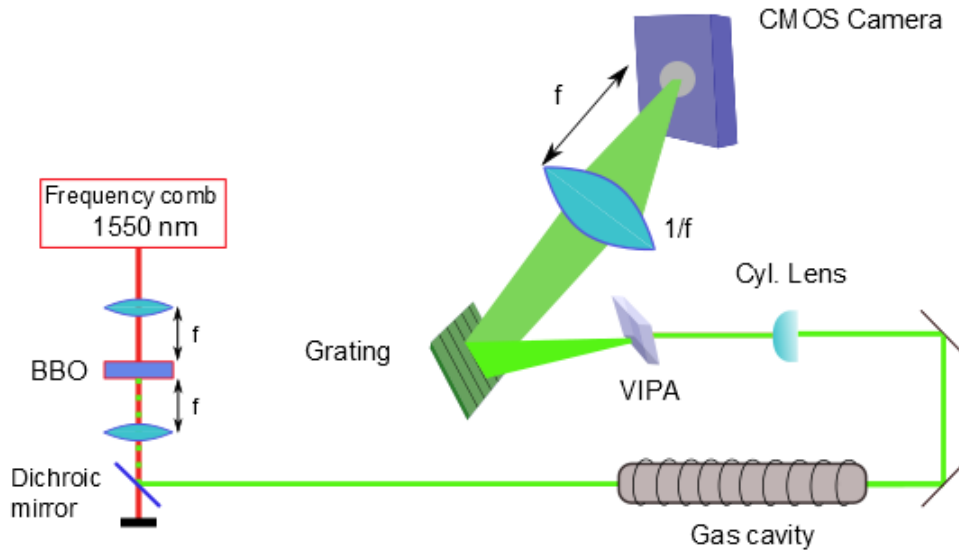


**Figure 3.2.:** Simplified setup for  $O_2$  detection branch

In the picture above we can see that the frequency comb is injected in a nonlinear crystal and the second harmonic generation (SHG) process is achieved. Two lenses are positioned before and after the crystal to respectively, focus inside the crystal and collimate the beam after the crystal. Then a dichroic mirror is introduced along the beam path to reflect the 760 nm part and transmit the 1550 nm residue. This wavelength is then suppressed with a beam dump.

Later on the beam pass through the gas cavity where it interacts with the gas inside the cavity and suffers absorption if it is filled with a mixture or a gas containing  $O_2$ .

After the cavity the purpose is to reveal the absorption and we intend to do that with the Virtually Imaged Phased Array (VIPA) spectrometer.

## 4. Light Source

The light source is a TOPTICA FemtoFERb 1560 Mode locked Er:fiber laser with a central wavelength of 1550 nm, 200 nm bandwidth and repetition rate of 100MHz.

Mode-locked fiber lasers are really performant for ultrashort pulse generation, and in fact it was discovered that a femtosecond mode-locked laser can actually be used for generating very broadband frequency combs. To accomplish our purpose of revealing O<sub>2</sub> lines we used a Beta Barium Borate (BBO) Nonlinear Crystal to achieve Second Harmonic Generation (SHG) at 760 nm. The output beam filtered from the original component at 1550 nm is the light source intended for the spectroscopy experiment. In this chapter we describe the Frequency Comb Laser and the SHG process deriving the most important parameters.

### 4.1. Frequency Comb Laser.

In these chapter the frequency comb laser principle is described as well as the unique characteristics that make the frequency comb so important for our measurements, focusing on the origin of the comb structure and the important parameters in order to understand and to control them.

#### 4.1.1. Frequency comb principle.

A frequency comb has a spectrum that consist of equidistant lines over a broad bandwidth (fig 4.1), and if the comb frequencies are known, the frequency comb can be used to measure unknown frequencies by measuring beat notes, which reveal the difference in frequency between the unknown frequency and the comb frequencies.

For performing such measurements in a wide frequency range, a large overall bandwidth of the frequency comb is needed.

The generation of a frequency comb requires that the periodicity applies not only to the pulse envelopes, but to the whole electric field of the pulses, so coherence between the pulses is required. The pulses can be produced once for every round trip of the light inside the cavity; then they are separated by a period  $\tau = \frac{n_r L}{c}$ , where  $L$  is the cavity length of the laser,  $n_r$  is the refractive index inside the cavity and  $c$  is the velocity of light. We can define the repetition rate of the laser as the inverse of this period  $f_{rep} = \frac{1}{\tau}$ .

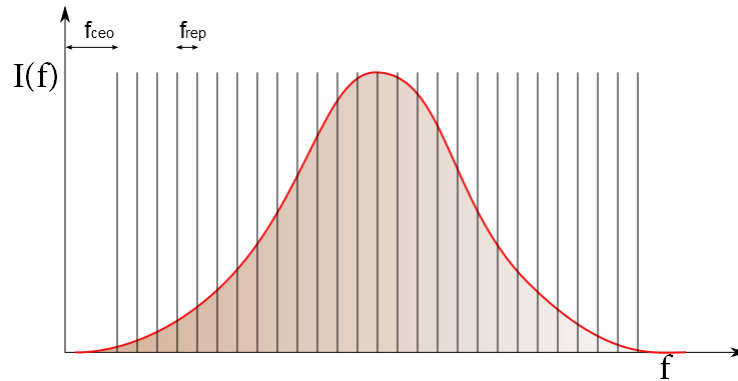


**Figure 4.1.:** Spectrum of a frequency comb, showing the frequency repetition rate  $f_{rep}$  and the frequency offset  $f_{ceo}$

If the cavity is filled with a non-dispersive medium, the refractive index is frequency independent and the frequencies of the longitudinal modes are just integer multiples of the repetition rate:

$$f_m = m f_{rep} ; \quad m = 1, 2, 3, \dots$$

When the cavity contains a dispersive medium the previous equation is still valid, but a frequency offset ( $f_0$ ) appears [12]. The origin of this offset lies in the difference between the group and phase velocities of the pulses. An individual pulse can be regarded as the product of an envelope function  $\hat{E}(t)$  and a continuous carrier wave of frequency  $\omega_c$  [5]. As illustrated in Figure 4.2 there can be a phase shift between the peak of the envelope and the closest peak of the carrier wave, this shift is commonly known as the carrier-envelope phase ( $\phi_{ce}$ ). The electric field of the pulse is then written as  $E(t) = \hat{E}(t)e^{i(\omega_c t - \phi_{ce})}$ . As the carrier propagates at the phase velocity and the envelope travels at the group velocity, the carrier-envelope phase can change from pulse to pulse.

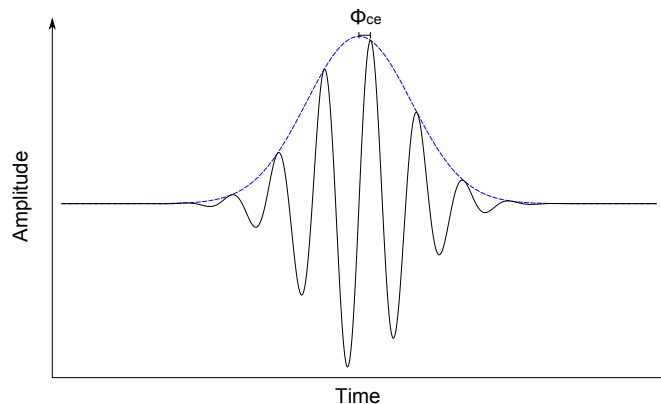


**Figure 4.2.:** Envelope and carrier of a pulse

If we consider the mode-locked pulses as the superposition of optical frequencies, we can write

$$E(z,t) = \text{Re} \left\{ \sum_m \left( E_m e^{j(\omega_m t - \beta_m z + \phi_m)} \right) \right\} \quad (4.1)$$

where  $E(z,t)$  is the electric field of our comb,  $\omega_m$  is the angular frequency,  $\beta_m$  is the propagation constant and  $\phi_m$  is the phase term. In addition  $z$  represent the position within the cavity, assumed as a ring cavity with length around the cavity  $L$ .

Unfolding the propagation constant assuming a linear behaviour we obtain:

$$\beta(\omega) = \beta_0 + \beta_1 \hat{\omega} \quad (4.2)$$

Here  $\beta_0 = \omega_0/v_p$  is the propagation constant and  $v_p$  is the phase velocity, both evaluated at a reference frequency  $\omega_0$ ,  $\hat{\omega}$  is the frequency offset from  $\omega_0$ , while  $\beta_1$  is the inverse of the group velocity  $v_g$ .

Combining expressions 4.2 and 4.1 it is possible to rewrite the electric field

$$E(z,t) = \text{Re} \left\{ e^{j(\omega_0 t - \beta_0 z)} \sum_m E_m e^{[\hat{\omega}_m(t - \beta_1 z) + \phi_m]} \right\} \quad (4.3)$$

Using the cavity resonance condition  $\beta_m L = 2m\pi$  we find that

$$\beta_m(\omega) = \beta_0 + \beta_1 \hat{\omega} = \frac{2m\pi}{L} \quad (4.4)$$

$$\hat{\omega} = \frac{2m\pi v_g}{L} - \frac{\omega_0}{v_p} v_g \quad (4.5)$$

If now we consider two modes indices  $m$  and  $p = m - m'$  where  $m'$  represents the index associated with  $\omega_0$  assumed to be one of the cavity resonances

$$\omega_{m+p} - \omega_m = \frac{2\pi p v_g}{L} = p \Delta\omega \quad \text{where} \quad \Delta\omega = \frac{2\pi v_g}{L} \quad (4.6)$$

Thus the frequency spacing is inversely proportional to the group delay  $T = L/v_g$ . We now assume the reference frequency  $\omega_0$  with mode index  $m'$  to be one of the cavity resonances, and the integer  $p = m - m'$  is the difference in mode indices between frequencies  $\omega_m$  and  $\omega_0$ . To simplify the notation we chose  $z=0$ , and we obtain for the mode-locked laser

$$E(z=0,t) = \text{Re} \left\{ e^{j\omega_0 t} e^{j\phi_{m'}} \sum_p E_{p+m'} e^{j(p\Delta\omega + \hat{\phi}_p)} \right\} \quad (4.7)$$

where  $\hat{\phi}_p = \phi_{p+m'} - \phi_m$ . In this way we can clearly distinguish the envelope and the carrier of

the electric field . If we now examine the carrier frequency we can derive from eq 4.4

$$\frac{\omega_0 L}{v_p} = 2\pi m' \quad (4.8)$$

Converting everything in terms of frequency spacing  $\Delta\omega$

$$\omega_0 = m'' \Delta\omega + \delta\omega \quad (4.9)$$

Where  $\delta\omega$  is the comb offset frequency and  $\delta\omega$  is chosen according to  $|\delta\omega| \leq \Delta\omega/2$ . Deriving  $\delta\omega$  from the equations 4.6 4.8 4.9 can be obtained

$$\delta\omega = \Delta\omega \left( \frac{v_p}{v_g} m' - m'' \right) \quad (4.10)$$

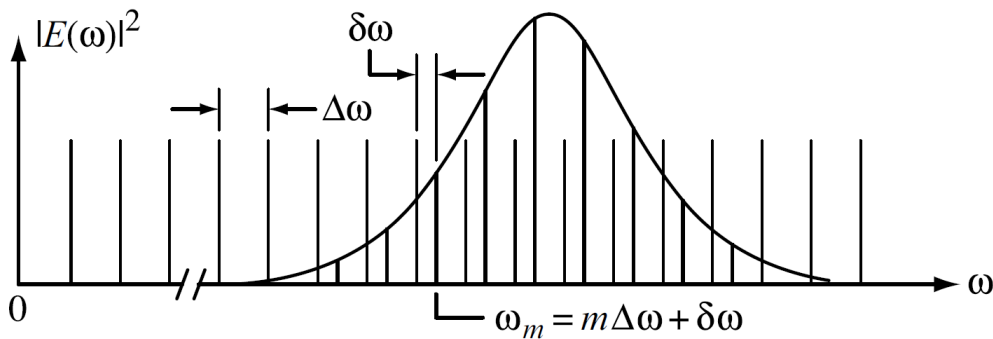


**Figure 4.3.:** Frequency comb spectrum [3]

When the phase and group velocities are equal, as in vacuum, the offset frequency is equal to zero,  $\delta\omega = 0$ . In this case when the comb of frequencies defined by  $n\Delta\omega + \delta\omega$ , with  $n$  an integer, is extended to low frequency, one of the comb frequencies falls precisely at zero. On the other hand, in real media the phase and group velocities generally differ, and the frequency comb is shifted by  $\delta\omega$  from an imaginary frequency grid with identical frequency spacing ( $\Delta\omega$ ) but passing through zero. Such a frequency comb with offset is illustrated in fig 4.3. In general, the frequencies of the individual comb lines may be written (in rad/s or hertz) as

$$\omega_m = m\Delta\omega + \delta\omega \quad (4.11)$$

$$f_m = m f_{rep} + f_{CEO} \quad (4.12)$$

with  $f_{rep} = 1/T$  is the pulse repetition frequency equal to the inverse of the period and  $f_{CEO} = \delta\omega/2\pi$  is the carrier-offset-frequency. If  $\delta\omega \neq 0$  the electric field can be seen in fig 4.4.

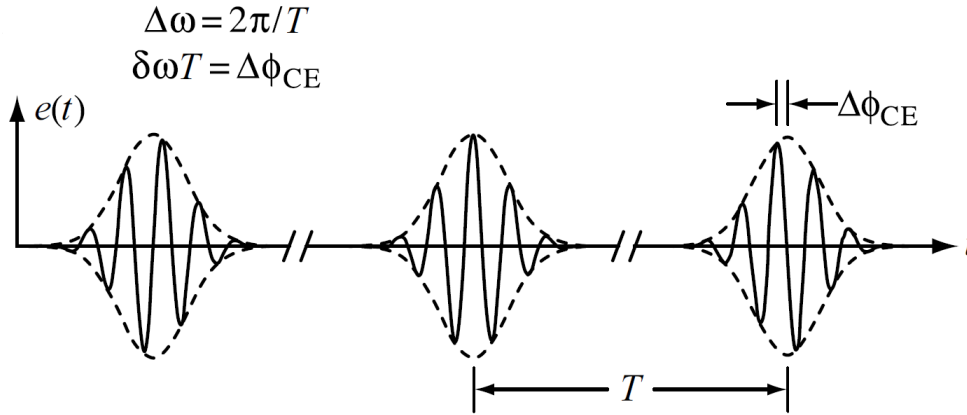


**Figure 4.4.:** Pulses train of a frequency comb [3], showing the  $\Delta\phi_{CE}$

So the electric field presents a part that is periodic plus an additional phase shift part  $\Delta\phi_{CE}$  accumulated on each pass through the laser given by

$$\Delta\phi_{CE} = \delta\omega T \quad (4.13)$$

If we examine the expression of the carrier-envelope-offset phase  $\Delta\phi_{CE}$ , we will arrive at some interesting results using equations 4.10, 4.8

$$\Delta\phi_{CE} = \frac{\omega_0 L}{v_g} - 2\pi m'' = \frac{\omega_0 L}{v_g} - \left( \frac{\omega_0 L}{v_p} - 2\pi m' \right) - 2\pi m'' \equiv \omega_0 \left( \frac{L}{v_g} - \frac{L}{v_p} \right) \quad (4.14)$$

In the last expression we have dropped the phase terms equal to integer multiples of  $2\pi$ , which are not physically meaningful. As a result, we find that the per-pass change in the carrier-envelope offset phase is determined by the difference between the per-pass group and phase delays. When the electric field is written in a retarded time frame traveling with the envelope (i.e., traveling at the group velocity), a phase term identical to that in the equation above must be included to account for the different propagation velocities of the carrier and the envelope.

### 4.1.2. Detection of the Carrier envelope offset frequency and stabilization

In order to stabilize the comb it is very important to measure as precisely as possible the carrier-envelope offset frequency  $f_{CEO}$ . A way of doing this is using the eq(4.12). In fact considering the second harmonics:

$$f_{2n} = 2n(f_{rep}) + f_{CEO} \quad (4.15)$$

$$2(f_n) = 2(nf_{rep} + f_{CEO}) \quad (4.16)$$

And make them interfere we have

$$2f_n - f_{2n} = f_{CEO} \quad (4.17)$$

So ideally just taking two components of the same spectrum and make them interfere we can achieve the  $f_{CEO}$ . Operatively the steps to stabilize the frequency comb are connected to the precise determination of both the frequency repetition rate  $f_{rep}$  and the  $f_{CEO}$ . As we can see in figure 4.5 the mode-locked laser beam is split and one part is sent onto a photodetector, producing an output signal that contains information about the frequency repetition rate. This signal is then compared to a Radio Frequency (RF) reference oscillator and the difference frequency output is used as feedback to lock the laser  $f_{rep}$  through appropriate electronics back to the laser. The other part of the beam is injected in a  $f - 2f$  interferometer. So the beam is again split, usually with a dichroic mirror, in order to divide the components with lower frequencies from the ones with higher frequencies. The branch with lower frequencies is usually sent through a non-linear crystal in order to achieve a SHG process. Now the second harmonic interferes with the branch of the beam with higher frequencies. This process reveals the  $f_{CEO}$  and again through a RF reference oscillator the frequency is locked to the laser through appropriate electronics. Due to the importance of this interference process we need a spectrum that can space an octave-span, like the one of a fiber laser.

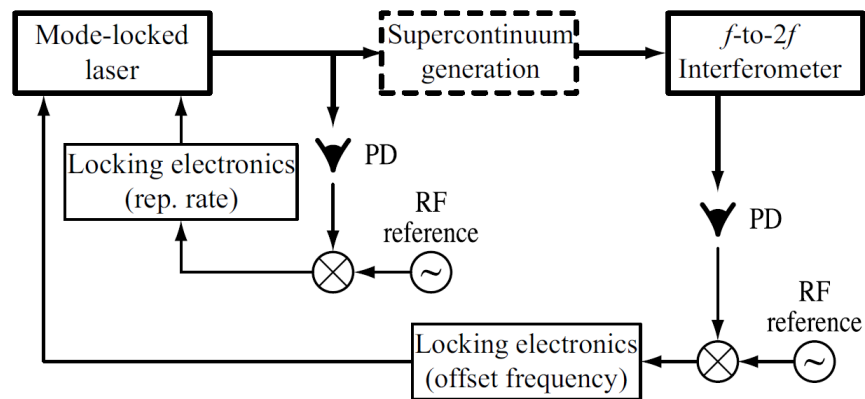


**Figure 4.5.:** Mode-locked laser frequency stabilization scheme

## 4.2. Second Harmonic Generation

In this project the original wavelength of the frequency comb laser used as light source was 1550 nm and the band was not broad enough to cover the right spectral region from 759 nm to 763 nm, so in order to fix this issue the second harmonic of the original comb was generated from a Beta Barium Borate nonlinear crystal. Here a short theoretical description of nonlinear effects that lead to Second Harmonic Generation (SHG) is given followed by the brief illustration of the experimental spectrum of the Second Harmonic beam after the nonlinear crystal.

### 4.2.1. Polarization Nonlinear effects

Nonlinear effects arise in materials, since the material response may be nonlinear with applied fields, and can couple back to the optical field, giving rise to nonlinear optics. In our treatment we take the optical polarization as the material response of interest. For low energy processes approximation, the polarization in the dielectric material is linearly proportional to the applied electric field. However since in 1960, when the coherent high intensity light source became available, people realized that the linearity is only an approximation. The polarization can be expanded in terms of applied electric field:

$$\mathbf{P} = \epsilon_0 \chi_e \mathbf{E} \quad (4.18)$$

where  $\mathbf{P}$  is the polarization,  $\chi_e$  is the susceptibility and  $\mathbf{E}$  is the applied electric field. The interaction of intense light with a nonlinear optical crystal creates a nonlinear polarization [13]:

$$\mathbf{P} = \epsilon_0 \left( \chi^{(1)} \mathbf{E} + \chi^{(2)} \mathbf{E}^2 + \chi^{(3)} \mathbf{E}^3 + \dots \right) \quad (4.19)$$

where the terms  $\mathbf{E}^2, \mathbf{E}^3, \dots$  represents the nonlinearity inside the polarization. The terms  $\chi^{(n)}$  are the nth order susceptibilities.

### 4.2.2. Second order effects

The reason why polarization fields are so important in second order effects is explained looking at the scalar wave equation in plane wave approximation

$$\frac{\partial^2 E}{\partial z^2} - \frac{n^2}{c_0^2} \frac{\partial^2 E}{\partial t^2} = \mu_0 \frac{\partial^2 P_L}{\partial t^2} + \frac{\partial^2 P_{NL}}{\partial t^2} \quad (4.20)$$



Where  $n$  is the refraction index,  $c_0$  the light velocity in vacuum,  $\mu_0$  the vacuum magnetic permittivity and  $P_L$  and  $P_{NL}$  the linear and nonlinear terms of the polarization.

The polarization is the reaction of the material to the wave propagation. But in this way it is possible to have charges inside the medium that can be accelerated, thus creating electromagnetic radiation that is not necessarily at the same frequency as the electric field.

Deriving the polarization components for second order effects ( $P = \epsilon_0 \chi^{(2)} E^2$ , part of eq 4.19) and considering an electric field with two frequency components, the electric field can be seen as

$$E(z, t) = \frac{1}{2} \left[ E_1 e^{i(\omega_1 t - k_1 z)} + E_2 e^{i(\omega_2 t - k_2 z)} + c.c \right] \quad (4.21)$$

The nonlinear polarization related to the second order is

$$P_{NL} = \epsilon_0 \chi^{(2)} E(z, t)^2 \quad (4.22)$$

From the interaction of an electric field made of two frequency components with a nonlinear crystal, it is possible to see four other new terms with different frequencies generated by the second order process:

Sum Frequency Generation	$\omega_1 + \omega_2$
Difference Frequency Generation	$\omega_1 - \omega_2$
Second Harmonic Generation	$2\omega_1, 2\omega_2$
Optical Rectification	zero-frequency term

The processes in fig 4.6 can arise when a laser of frequency  $\omega$  is injected into a nonlinear crystal with proper energy levels matching the wavelength of the laser. The purpose of this thesis is not to derive all the previous processes, the derivation can be found in [3].

The only term of interest is the one connected to the Second Harmonic Generation (SHG), a coherent optical process of radiation of dipoles in the material, dependent on the second term of the expansion of polarization. The Second Harmonic Generation process creates a photon with frequency  $2\omega$ , after the crystal, starting with two photons at frequency  $\omega$  before the crystal.

### 4.2.3. Derivation of SH field

In this subsection it is provided a mathematical derivation of the Second Harmonic field considering the process happening in a nonlinear medium. The medium is treated as lossless both at frequency  $\omega$  and  $2\omega$  to simplify the calculations. We start from the scalar waves equation in plane wave approximation (eq 4.20)

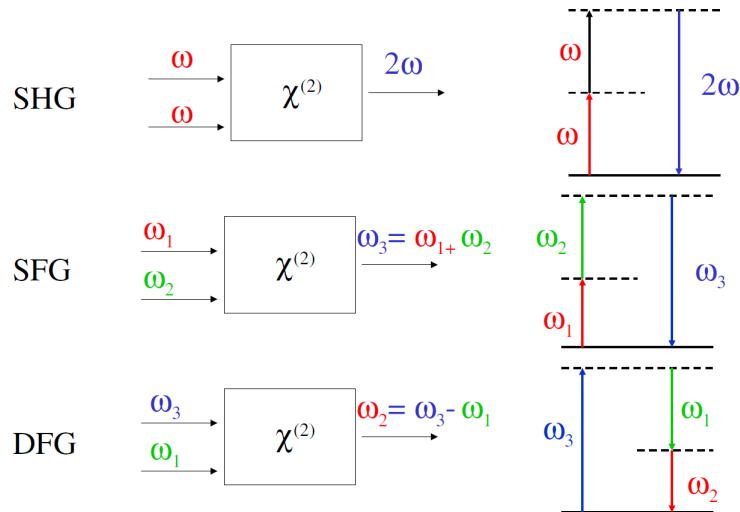


**Figure 4.6.:** In this picture are illustrated the processes that derive from the expansion of the second order term of the nonlinear polarization. Second Harmonic Generation, Sum Frequency Generation and Difference Frequency Generation.

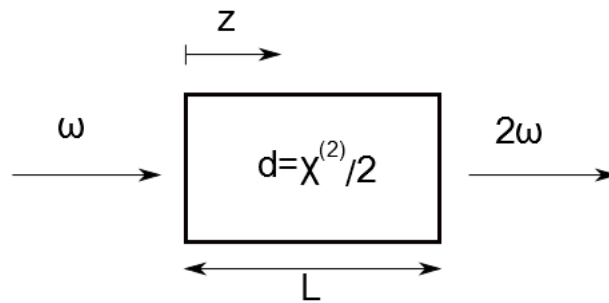


**Figure 4.7.:** Schematic of the second harmonic process in a nonlinear lossless medium

$$\frac{\partial^2 E}{\partial z^2} - \frac{1}{c_0^2} \frac{\partial^2 E}{\partial t^2} = \mu_0 \frac{\partial^2 P_L}{\partial t^2} + \mu_0 \frac{\partial^2 P_{NL}}{\partial t^2} \quad (4.23)$$

Expanding  $P_{NL}(z, t)$  and  $E(z, t)$

$$P_{NL}(z, t) = p_{NL}(z, t) e^{i\omega_0 t - ik_p z} \quad (4.24)$$

$$E(z, t) = A(z, t) e^{i(\omega_0 t - k_0 z)} \quad (4.25)$$

where  $p_{NL}(z, t)$  and  $A(z, t)$  are the envelopes of  $P_{NL}$  and  $E(z, t)$ . To keep the notation simple, we use the scalar notation for the electric field, the nonlinear susceptibility, and the nonlinear polarization.

Now calculating the first and second derivative of  $P_{NL}$

$$\frac{\partial P_{NL}}{\partial t} = \left[ \frac{\partial p_{NL}}{\partial t} + i\omega_0 p_{NL} \right] e^{i(\omega_0 t - k_p z)} \quad (4.26)$$

$$\frac{\partial^2 P_{NL}}{\partial t^2} = \left[ \frac{\partial^2 p_{NL}}{\partial t^2} + i2\omega_0 \frac{\partial p_{NL}}{\partial t} - \omega_0^2 p_{NL} \right] e^{i(\omega_0 t - k_p z)} \quad (4.27)$$

For the slowly varying envelope approximation (SVEA) it is possible to write

$$\left| \frac{\partial^2 p_{NL}}{\partial t^2} \right| \ll \left| i2\omega_0 \frac{\partial p_{NL}}{\partial t} \right| \ll \left| \omega_0^2 p_{NL} \right| \quad (4.28)$$

So the second derivative of the nonlinear polarization is

$$\frac{\partial^2 P_{NL}}{\partial t^2} = -\omega_0^2 p_{NL} e^{i(\omega_0 t - k_p z)} \quad (4.29)$$

Now equation 4.23 become

$$\frac{\partial^2 E}{\partial z^2} - \frac{1}{c_0^2} \frac{\partial^2 E}{\partial t^2} = \mu_0 \frac{\partial^2 P_L}{\partial t^2} - \omega_0^2 p_{NL} e^{i(\omega_0 t - k_p z)} \quad (4.30)$$

Following the same calculations of B we have the parabolic equation for the nonlinear polarization:

$$-\frac{2ik_0 \partial A}{\partial z} - \frac{2ik_0}{v_{g0}} \frac{\partial A}{\partial t} + k_0 GVD \frac{\partial^2 A}{\partial t^2} = -\mu_0 \omega_0^2 p_{NL} e^{-i\Delta k z} \quad (4.31)$$

where  $GVD$  is the group velocity dispersion,  $v_{g0}$  the group velocity and  $\Delta k = k_{2\omega} - 2k_\omega$  is the wavevector phase mismatch. We can rewrite the equation dividing for  $-2ik_0$  having

$$\frac{\partial A}{\partial z} + \frac{1}{v_{g0}} \frac{\partial A}{\partial t} - \frac{i}{2} GVD \frac{\partial^2 A}{\partial t^2} = -i \frac{\mu_0 \omega_0 c}{2n_0} p_{NL} e^{-i\Delta k z} \quad (4.32)$$

the first term of the equation regards the linear effects, while the second term regards the nonlinear effects connected to the nonlinear polarization.

The total electric field is written in eq 4.21 and assuming to enter the medium only with  $\omega$ , we can write the nonlinear polarization both for the  $\omega$  and  $2\omega$  components.

$$P_{NL}^{\omega} = \varepsilon_0 \frac{\chi^{(2)}}{4} 2A_{\omega}^* A_{2\omega} e^{i[(2\omega-\omega)t - (k_{2\omega}-k_{\omega})z]} + c.c. \quad (4.33)$$

$$P_{NL}^{2\omega} = \varepsilon_0 \frac{\chi^{(2)}}{4} 2A_{\omega}^2 e^{i[(\omega+\omega)t - 2k_{\omega}z]} + c.c. \quad (4.34)$$

Using equation 4.24 and substituting into the expression of 4.32 the result are two coupled equations

$$\frac{\partial A_{\omega}}{\partial z} + \frac{1}{v_{g\omega}} \frac{\partial A_{\omega}}{\partial t} - \frac{i}{2} GVD \frac{\partial^2 A_{\omega}}{\partial t^2} = -i \frac{\mu_0 \omega c}{2n_{\omega}} \varepsilon_0 \frac{\chi^{(2)}}{4} 2A_{\omega}^* A_{2\omega} e^{-i(k_{2\omega}-k_{\omega}-k_{\omega})z} \quad (4.35)$$

$$\frac{\partial A_{2\omega}}{\partial z} + \frac{1}{v_{g2\omega}} \frac{\partial A_{2\omega}}{\partial t} - \frac{i}{2} GVD \frac{\partial^2 A_{2\omega}}{\partial t^2} = -i \frac{\mu_0 2\omega c}{2n_{2\omega}} \varepsilon_0 \frac{\chi^{(2)}}{4} 2A_{\omega}^2 e^{i(k_{2\omega}-2k_{\omega})z} \quad (4.36)$$

At this point the term with the group velocity  $v_{gi}$  and the Group Velocity Dispersion (GVD) can be drop considering the SVEA. The coupled equations now are

$$\begin{cases} \frac{\partial A_{2\omega}}{\partial z} = -ib_{2\omega} (A_{\omega})^2 e^{i\Delta kz} \\ \frac{\partial A_{\omega}}{\partial z} = -ib_{\omega} A_{\omega}^* A_{2\omega} e^{-i\Delta kz} \end{cases} \quad (4.37)$$

where  $\Delta k = k_{2\omega} - 2k_{\omega}$  and  $b_i = \frac{\omega_i d_{eff}}{2nc}$  and  $d_{eff} = \chi^{(2)}/2$ . The effective nonlinear coefficient  $d_{eff}$  takes into account the tensor products of the fields and the nonlinear susceptibility tensor. For lossless nonlinear media,  $d_{eff}$  is real [13].

We assume that  $\Delta k = 0$ , this phase matching condition is usually required for efficient harmonic generation. In addition we assume that the  $2\omega$  wave remains much weaker than the input wave. So it is possible to write

$$|A_{2\omega}(z)| \ll |A_{\omega}(0)| \quad (4.38)$$

In this way we ignore the depletion of the input wave and  $A_{\omega}$  is taken constant throughout the medium. The equations become

$$\begin{cases} \frac{\partial A_{2\omega}}{\partial z} = -ib_{2\omega} (A_{\omega,0})^2 \\ A_{\omega}(z) \approx A_{\omega,0} \end{cases} \quad (4.39)$$

Assuming that the component at  $2\omega$  is zero in input the solution is:

$$A_{2\omega}(z) = -ib_{2\omega}(A_{\omega,0})^2 z \quad (4.40)$$

Switching to intensity

$$I_{2\omega} = \Gamma^2 I_{\omega}^2 L^2 \quad (4.41)$$

$$\Gamma = \frac{2b^2}{\epsilon_0 c n} \quad (4.42)$$

The intensity of SH component depends on the square intensity of the fundamental. This derivation is correct only in the low conversion efficiency limit.

In case of phase matching but arbitrary pump depletion and assuming  $A_{2\omega}(0) = 0$  and  $A_{\omega}(0) = 1$  the solutions are [13]

$$\begin{cases} A_{2\omega}(\zeta) = -iA_{\omega}(0)\tanh(bA_{\omega}(0)\zeta) \\ A_{\omega}(\zeta) = A_{\omega}(0)\operatorname{sech}(bA_{\omega}(0)\zeta) \end{cases} \quad (4.43)$$

According to the phase matching condition  $b_{\omega}=b_{2\omega}=b$  [13]  
The solutions are here displayed in fig:4.8

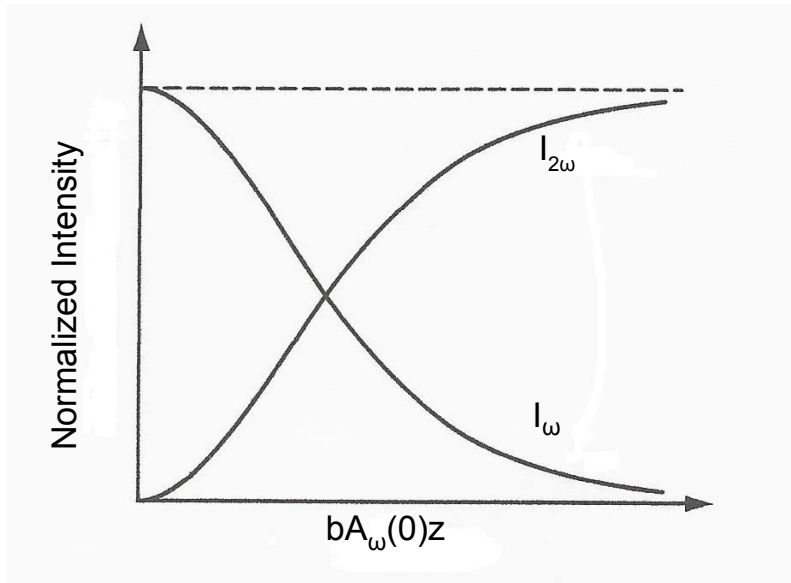


**Figure 4.8.:** Normalized intensity of fundamental and second harmonic components in continuous wave, with plane wave approximation and phase matching condition  $\Delta k = 0$

The picture shows that to the first order in the input field the solution resembles the one for

undepleted pump solution, while for higher input fields the second harmonic intensity is growing and at the same time the input field is decreasing leading to a saturation behaviour of the second harmonic. In the approximation of  $bA_{\omega}(0)z \ll 1$ , the input field is ideally completely converted into second harmonic field.

It is also possible to derive the expressions for arbitrary  $\Delta k$  [14] but that goes beyond the scope of this thesis.

### 4.3. Light source characterization

In order to proceed with the experiments we characterized the output spectrum of the nonlinear crystal thanks to a HP – 8562A spectrum analyzer and the profile is shown in fig 4.9.

As we can see the spectrum has three peaks around respectively 788 nm, 773 nm, 760 nm.

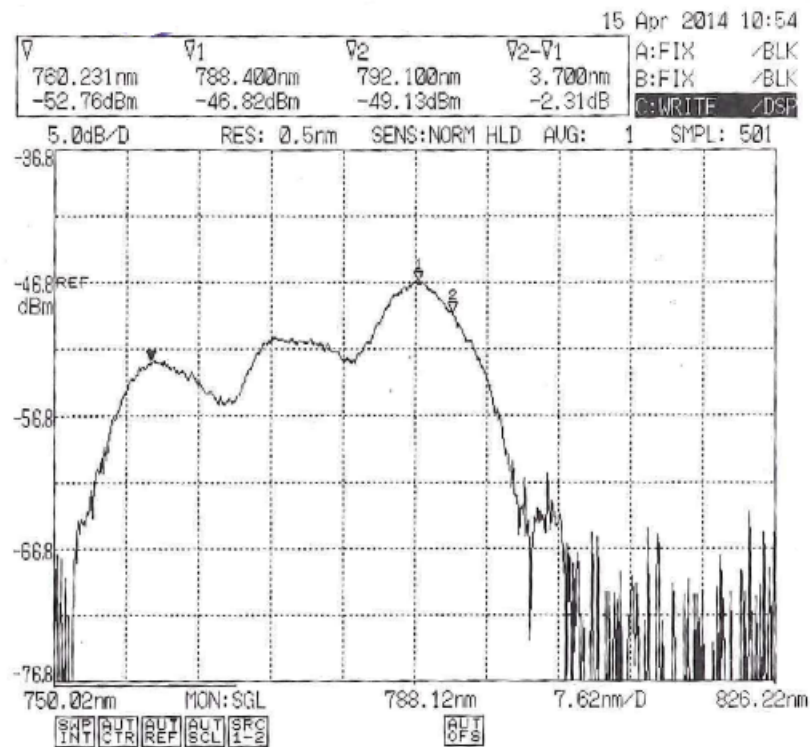


**Figure 4.9.:** Spectrum of second harmonic generation after BBO crystal

The O<sub>2</sub> absorption lines are around the peaks of 760 nm, the lower one for intensity, precisely 6dB less than the higher one. Though it would have been better to have more power on the window of interest we are confident absorption is detectable with this output profile of the second harmonic beam.

# 5. VIPA Spectrometer

The most important part of our setup is the VIPA Spectrometer illustrated in fig 5.1. The main task we want achieve with the VIPA spectrometer is to obtain the spectrum of the incoming beam, and to follow this target we need to know the intensity distribution on the CMOS detector plane, placed at the back focal plane of a spherical lens 5.1.

The VIPA spectrometer has a high spectral resolution over a wide bandwidth [1]. This spectrometer has a resolution of 800 MHz at central frequency of 760 nm over a bandwidth of 200 nm. The VIPA spectrometer is made of two stage, the first consists in the vertical separation of the frequencies, spatially, operated by the etalon of a Vertical Imaged Phased Array (VIPA), the second stage consists in the separation of the mode of the VIPA's etalon operated by a diffraction grating.

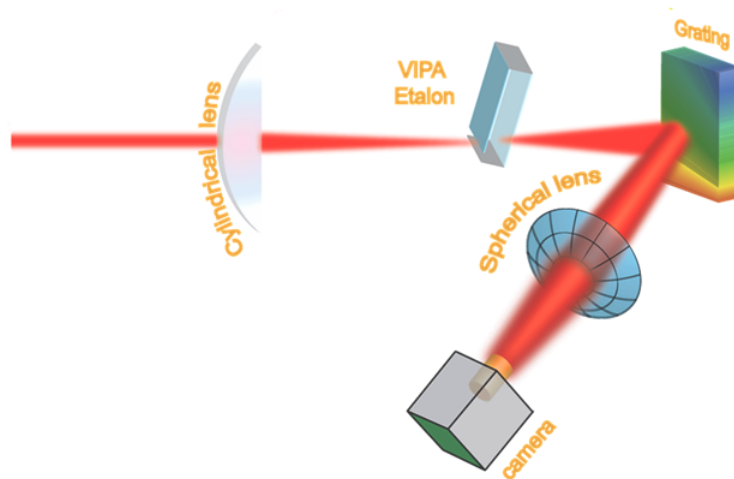


**Figure 5.1.:** VIPA spectrometer components [1]. The VIPA spectrometer is made of a cylindrical lens that is focusing the beam on the bottom part of the VIPA etalon, after the etalon the beam proceed towards the grating that is dispersing the spectral components in several orders and through a spherical lens is focusing onto a CMOS camera

The VIPA etalon is an optical element which shows a large angular dispersion over wavelength change. It consists of a semi-cylindrical lens and a thin glass plate with proper reflection coatings. The beam is focusing on the VIPA etalon (Virtually Imaged Phase Array) with high accu-



racy thanks to a 3D translation stage and a semi-cylindrical lens with focal length of 10 cm. The etalon is used to spatially separate the frequencies in the vertical direction with a high resolution. A diffraction grating is introduced to separate the modes of the VIPA etalon in the horizontal direction. The purpose of the grating is to enhance the separation between the modes of the VIPA etalon in order to allow the detection. After the grating a spherical lens with focal of 40 cm helps to focus the beam on the CMOS camera. The spherical lens is mounted on a 3D translation stage to facilitate the focusing process and to correct misalignments.

The diffractions from the VIPA and the grating are spatially separated so we can treat them one at a time describing more in detail the VIPA etalon and the diffraction grating.

## 5.1. VIPA etalon

The VIPA etalon can be seen like a combination of a Fabry-Perot and a diffraction grating for its properties [15]. It is a thin glass plate covered on each side by reflective coating with different reflectivities. The back plate has a reflective coating with a reflectivity of  $R = 0,95$ , the front plate has reflectivity of  $R = 0,999$  everywhere but at the bottom, where under a visible horizontal stripe an Antireflecting Coating (AR) is applied to allow the radiation to couple in.

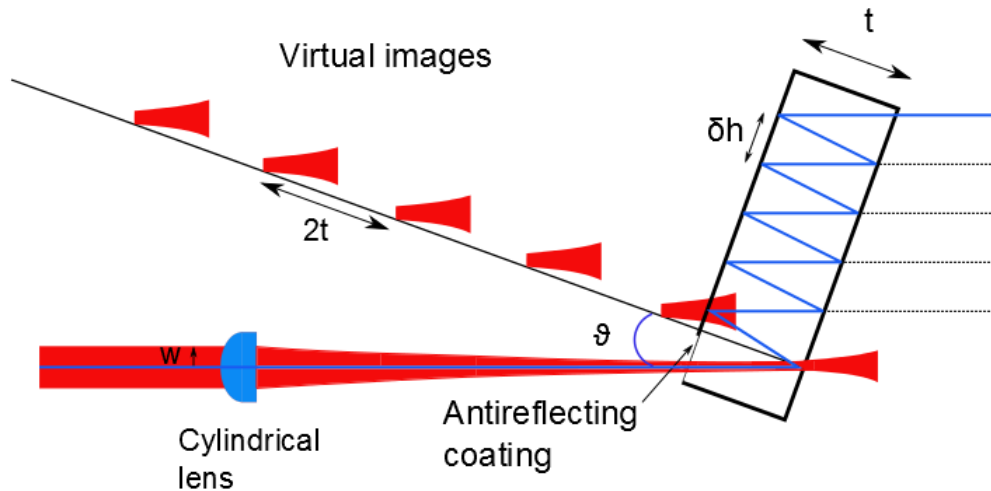


**Figure 5.2.:** VIPA etalon. In this picture is shown the angle  $\theta$  between the incident beam and the normal to the VIPA, where the virtual images are lying.

An interesting feature about the VIPA etalon is shown in fig 5.2. In fact the beam fractions that come from each reflection inside the etalon can be seen as if coming from a virtual source that lies on the normal to the etalon itself, and the distance between two sources is equal to  $2t$ , where

$t$  is the thickness of the etalon plate [16].

The etalon has an inclination with respect to the incident beam of an angle  $\alpha$  that can vary between  $1.5^\circ < \alpha < 3.5^\circ$ . In our case the angle was fixed at  $2^\circ$ . The angle of incidence  $\theta_{in}$  is related to the angle  $\theta_{et}$  from eq 5.4 and the smaller the angle  $\theta_{et}$  the bigger the amount of reflections inside the etalon.

The number of reflections should be not too high otherwise the frequencies related to the etalon modes in output are too overlapped to be solved, but not too low otherwise the output power is not enough to detect the beam [5].

Another operative characteristic of the VIPA is illustrated in figure 5.3. It is possible to see that the different wavelengths are angularly separated, but each of them is a collimated beam.

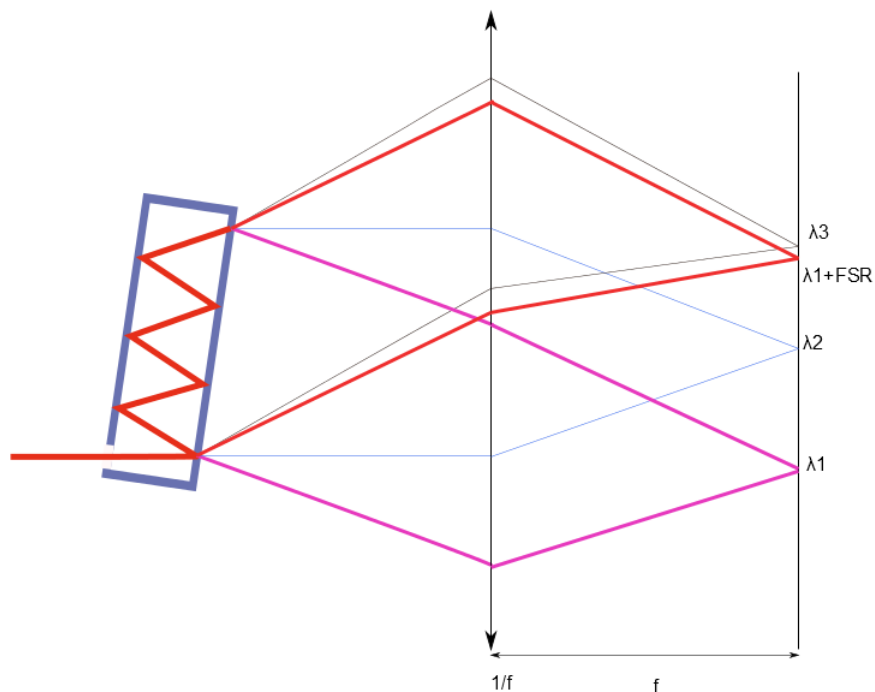


**Figure 5.3.:** VIPA etalon disperse the frequencies in different angles on the vertical line, but all of them considered separately are collimated beams

So if an ideal lens would be put after the VIPA etalon, on its focal plane all the wavelengths would be focused in a different spot. The problem is that there are also several orders for each wavelength, and different orders of different wavelengths are overlapped in the vertical direction after the VIPA. Introducing the grating we spread these wavelengths also in horizontal direction and looking just at one order of the grating we obtain the spectral informations without cross-talk.

## 5.2. VIPA parameters

After the operating description of the VIPA spectrometer in this section we give some parameters to show the potential of this spectrometer.

The first parameter of interest is the coupling efficiency. The entrance window of the etalon is really small and to calculate the coupling efficiency we need to know the beam input size  $w_e$  and the distance between two reflections  $\delta h$  on that side. The formula is [1]:

$$CE = \frac{P_{coupled}}{P_{incident}} = \left[ 1 - e^{-\left(\frac{\delta h/2}{w_e}\right)^2} \right]^2 \quad (5.1)$$

If we assume the incoming light is a Gaussian beam, then we can take  $w_e$  as the  $1/e$  radius of the the beam at the input window, which is given by

$$w_e = \frac{f_c \lambda_c}{\sqrt{2\pi} w} \quad (5.2)$$

where  $f_c$  is the focal length of the cylindrical lens,  $\lambda_c$  is the central wavelength of the incoming beam and  $w$  is the radius of the collimated beam prior to the cylindrical lens.

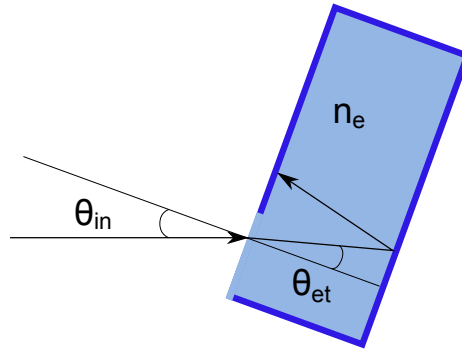


**Figure 5.4.:** Incident beam refracted inside the etalon and reflected at his rear plate

From Figure 5.4 we get the value of  $\delta h$  using geometrical optics [17]

$$\delta h = 2t \tan(\theta_{et}) \quad (5.3)$$

with  $\theta_{et}$  the angle inside the etalon, which is related to the incident angle  $\theta_{in}$  in this way:

$$n_{air} \sin(\theta_{in}) \approx \sin(\theta_{in}) = n_{et} \sin(\theta_{et}) \quad (5.4)$$

where  $n_{et}$  is the refractive index of the VIPA etalon.

The theory of the VIPA etalon has already been studied in detail, and here we chose to follow the master equation for propagation of a beam through VIPA spectrometer illustrated by Xiao *et al* [18].

$$I_{vipa}(y, \omega) \propto I_{in}(\omega) e^{\frac{-2f_c^2 y^2}{f^2 w^2}} \frac{1}{(1 - Rr)^2 + 4Rr \sin^2(\frac{\Delta}{2}k)} \quad (5.5)$$

here  $I_{in}(\omega)$  is the power spectral density of the input beam,  $f$  is the focal length of the spherical lens,  $f_c$  is the focal length of the cylindrical lens,  $w$  is the incident beam radius,  $y$  is the vertical coordinate in the detection plane,  $R$  and  $r$  are the front and rear reflectivity,  $k$  is the wavenumber, which is related to the wavelength by  $k = \frac{2\pi}{\lambda}$ .

This equation is the result of the product between the grating dispersion along x-direction and the VIPA dispersion along y-direction [18].

The parameter  $\Delta$  is defined by the relation [5]

$$\Delta = 2tn_{et} \cos(\theta_{et}) - 2t \frac{\tan(\theta_{et}) \cos(\theta_{in})y}{f} - t \frac{\cos(\theta_{et})y^2}{n_{et}f^2} \quad (5.6)$$

where  $n_{et}$ ,  $\theta_{et}$  are the etalon index of refraction and the angle refracted inside the VIPA and  $t$  is the etalon thickness.

Starting from equation 5.5 is possible to derive [1]:

- the spatial dispersion of light at the detection plane
- the spectral resolution of the VIPA
- the size of the interference pattern at the detection plane.

The spatial dispersion is telling us how big is the displacement we expect on the detection plane between two wavelengths. The spatial dispersion of the light at the detection plane is:

$$\frac{\Delta\lambda}{\Delta y} = \frac{-2t}{mf} \left[ \tan(\theta_{et}) \cos(\theta_{in}) + \frac{\cos(\theta_{et})y}{n_{et}f} \right] \quad (5.7)$$

with  $m \approx 2tn_{et} \cos(\theta_{et}/\lambda_c) = 8330$

The spectral resolution of the VIPA is giving us the smallest line we can resolve with the VIPA spectrometer and the formula is:

$$\delta\nu_{FWHM} = \frac{c(1-Rr)}{\pi\Delta\sqrt{Rr}} \quad (5.8)$$

The other parameter that is very important is the size of the VIPA *FSR* on the CMOS camera. In fact it is important to know how big the *FSR* should be to check if the detector is adapt to cover one *FSR* and so reveal the interference pattern in the correct way.

The size of the interference pattern at the detection plane is [5]:

$$\Delta y_{FSR} = \frac{mf\lambda_c^2 FSR}{2tc} \left[ \tan(\theta_{et}) \cos(\theta_{in}) + \frac{\cos(\theta_{et})y}{n_{et}f} \right]^{-1} \quad (5.9)$$

### 5.3. Diffraction grating

In order to resolve all the frequencies a grating was introduced. To have a complete and clear image of the *FSR* on the CMOS camera the grating is needed.

The grating is a blazed grating and is spreading the frequencies along horizontal direction.

Blazed gratings are particular type of diffraction gratings. They are optimized to achieve maximum grating efficiency at a particular order, in our case the order is  $m = 1$ .

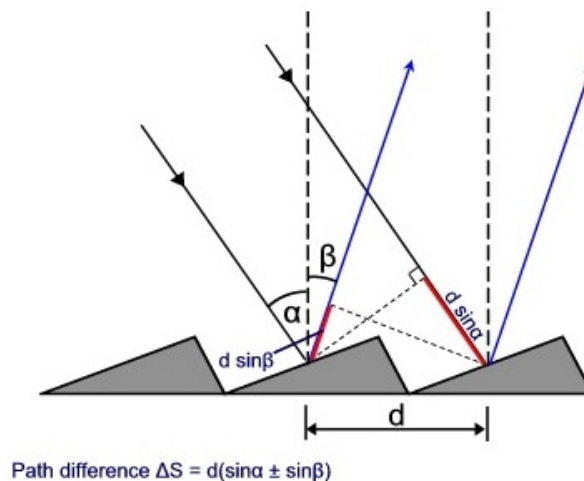


**Figure 5.5.:** Schematic of a blazed grating illustrating peculiar angles and distances [4]

The grating together with the spherical lens and the CMOS camera can be considered as a grating spectrometer and it is possible to calculate the spatial dispersion, spectral resolution and intensity distribution on the detection plane of the CMOS camera.

The picture 5.5 shows that the beam is hitting the grating with an incident angle  $\alpha$  and is reflected to an angle  $\beta$ . The diffracted angle of the light  $\beta$  is determined by the grating line-spacing  $d$ , the wavelength of the incident light  $\lambda$ , and the incident angle of the beam  $\alpha$  and is given from [19]:

$$m\lambda = d(\sin \alpha - \sin \beta) \quad (5.10)$$

where  $m$  is an integer, order of the diffracted light.

If we solve the equation for  $\beta$ :

$$\beta = \arcsin \left( \frac{m\lambda + d \sin \alpha}{d} \right) \quad (5.11)$$

Differentiating with respect to the wavelength  $\lambda$ :

$$\frac{d\beta}{d\lambda} = \frac{1}{\sqrt{1 - \left(\frac{m\lambda + d \sin \alpha}{d}\right)^2}} \frac{m}{d} = \frac{1}{\sqrt{1 - \sin^2 \beta}} \frac{m}{d} \quad (5.12)$$

using eq 5.10 to reduce  $m\lambda + d \sin \alpha = d \sin \beta$  and replacing  $1 - \sin^2(\beta) = \cos^2(\beta)$  we obtain the expression for the angular dispersion of light diffracted from the grating:

$$\Delta\beta = \frac{m}{d \cos \beta} \Delta\lambda \quad (5.13)$$

Next is the spatial separation of the frequencies at the CMOS camera (focal plane), that can be found using an imaging relation from Fourier optics  $\Delta x = f \Delta\beta$  [19], [5]:

$$\frac{\Delta\beta}{\Delta\omega} = \frac{\lambda^2 f}{2\pi c d \cos \beta} \quad (5.14)$$

here the differential relation was converted from wavelength to angular frequency using:

$$\Delta\lambda = -\frac{\lambda^2}{2\pi c \Delta\omega} \quad (5.15)$$

and the order of the grating assumed  $m = 1$ .

The radius of a focused monochromatic beam on the CMOS camera depends on the diameter of the incident beam  $w$ , the focal length of the lens  $f$ , the wavelength  $\lambda$  and the incident and diffracted angles from the grating  $\cos \alpha$ ,  $\cos \beta$  [20]:

$$w_0 = \frac{\cos \alpha}{\cos \beta} \frac{f \lambda}{\pi w} \quad (5.16)$$

At this point is possible to use equations 5.14, 5.16 and have the intensity distribution of light on the CMOS camera:

$$I_{CMOS}(x, \omega) \propto I_{inc} e^{-\frac{2 \left( x - \frac{\Delta \beta}{\Delta \omega} \bar{\omega} \right)^2}{w_0^2}} \quad (5.17)$$

where  $\bar{\omega} = \omega - \omega_0$ , considering  $\omega_0$  is the frequency at the center of the CMOS.

The resolution of the gratings is usually on the order of hundreds of GHz or several THz. To calculate the resolution of our grating, we assumed that two spots need to be separated of a distance that is  $1/e^2$  of the beam diameter, so [1]:

$$\Delta \nu_{min} = \frac{2cd}{\pi w \lambda} = 114 \text{ GHz} \quad (5.18)$$

with  $d = 0.91 \mu\text{m}$ ,  $w = 2 \text{ mm}$ ,  $\lambda = 760 \text{ nm}$ .

Usually is very difficult reach the resolution limit, but for sure the most important things to remember to achieve the better resolution possible are to align as well as possible the spherical lens in order to avoid aberrations, and to make sure the diffraction limited spot is larger than the pixel pitch such that at least two pixel can detect the spot and the CMOS is not limiting the measurements [5].

## 5.4. Numerical values of the spectrometer characteristics

Now we move on and give some numerical values for the spectrometer so that is possible to understand what the spectrometer can resolve.

The resolution of the VIPA is found using equation (5.8)

$$\delta \nu_{FWHM} = 690.7 \text{ MHz} \quad (5.19)$$

Evaluating the  $\Delta\lambda_{RES}$ , and  $\Delta\lambda_{FSR}$  we have

$$\Delta\lambda_{RES} = \frac{\lambda_c^2 \delta_{FWHM}}{c} = 1.34 \cdot 10^{-3} \text{ nm} \quad (5.20)$$

$$\Delta\lambda_{FSR} = \frac{\lambda_c^2 FSR}{c} = 9.62 \cdot 10^{-2} \text{ nm} \quad (5.21)$$

These results show that the  $FSR$  is bigger than the resolution of

$$\frac{9.62 \cdot 10^{-2} \text{ nm}}{1.34 \cdot 10^{-3} \text{ nm}} = 71.79 \quad (5.22)$$

So this should be enough to image the entire  $FSR$ . To have the best approximation possible to the spectral resolution is important to take into account also the pixel size, especially if the diffracted beam size is smaller than the pixel size. For that reason we calculated the influence of the pixel size as the frequency interval corresponding to one pixel width [5]

$$\delta\nu_p = \frac{2l_p t c}{\lambda^2 m f} \tan(\theta_{et}) \cos(\theta_{in}) = 14.157 \text{ MHz} \quad (5.23)$$

To see if the spectral resolution is affected by the pixel size we now add the square powers of 5.23 and 5.19 and then operate the square root:

$$\sqrt{(14.157 \text{ MHz})^2 + (690.7 \text{ MHz})^2} = 690.84 \text{ MHz} \quad (5.24)$$

The final result is a total resolution of 690.84 MHz, which is a really small deviation from the value of  $\delta\nu_{FWHM}$  and so we are confident that the effect of the pixel's size is minimum.

The CMOS detector we are using has a pixel size of  $2.2 \mu\text{m}$  and 1944 pixel so the height is of 4.4mm. In this sense is important to have the detector that can cover the whole FSR. The next calculation is about the size of the FSR on the detector plane. First we calculate the size of the interference pattern on the detection plane

$$W_y = \frac{\sqrt{2} f w}{f_c} = 3.14 \text{ mm} \quad (5.25)$$

where  $f_c$  is the cylindrical lens focal, and  $w$  is the input beam size.

Now if we calculate the drop of intensity at the edge of the detector compared to the centre of the image the result is

$$e^{\frac{-4.4}{3.14}} \approx 24.6\% \quad (5.26)$$

So we have just 24.6% intensity drop from the centre to the edge of the detector. Instead for what regards the size of the  $FSR$  on the detector, from equation (5.9) we obtain



$$\Delta y_{FSR} = 4.4 \text{ mm} \quad (5.27)$$

So according to the calculation we have the detector is good to cover an entire FSR. This guarantees we can record the complete  $FSR$  of the VIPA inside the camera and we also have extra space to see the repetition of the patterns and calibrate the spectrometer.

In table 5.2 are listed the parameters of the VIPA etalon, the gratings, the lenses, the input beam and the camera we use.

Element	Parameter		
VIPA etalon	Refractive index	$n_{et}$	1.81
	Thickness	$t$	1.75 mm
	Input side reflectivity	$R$	99.5 %
	Output side reflectivity	$r$	95.0 %
	Free Spectral Range	$FSR$	50 GHz
	Tilt	$\theta_{in}$	$2^\circ$
Grating	Groove's size	$d$	$0.91 \mu\text{m}$
	Incident angle	$\alpha$	$80^\circ$
Lenses	Cylindrical	$f_c$	100 mm
	Spherical	$f$	400 mm
Incident beam	Radius	$w$	2 mm
	Central wavelength	$\lambda_c$	760 nm
Camera	Number of pixels	$N_h \times N_v$	$2592 \times 1944$
	Pixel size	$l_p$	$2.2 \mu\text{m}$

**Table 5.1.:** VIPA spectrometer parameters.

## 5.5. Guideline for Alignment

The purpose of this section is to give some guideline for alignment of the VIPA spectrometer. The VIPA spectrometer is very sensitive to alignment and to have good measurements an optimal alignment is fundamental. A detailed explanation of how to align can be found in [5]. Here we just describe the main steps to clarify how alignment was performed.

In the first step we check the height of the beam and the angle of the VIPA etalon. To check the height of the beam is useful to send the beam through the etalon and aim for half power after it, keeping the beam parallel to the optical table. In this way the beam will fall half on the AR coating and half on the HR coating. The reflected part can give us a feedback about the inclination angle of the etalon. In fact looking at the picture 5.6, it is possible to calculate  $\Delta y$  in this way

$$\Delta y = \Delta z \tan(2\theta) \quad (5.28)$$

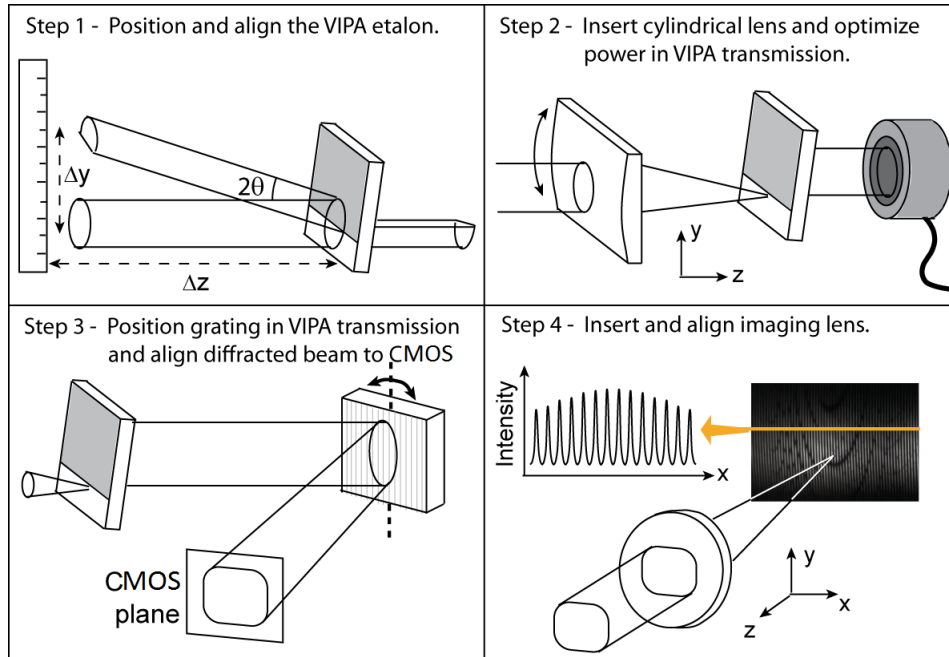


**Figure 5.6.:** Main steps for rough alignment of the VIPA spectrometer [5]

If the etalon is mounted on a translation stage, it is possible to fix the angle at the value that is most suitable for the experiment between  $1.5^\circ - 3.5^\circ$ .

In the second step the cylindrical lens is introduced in front of the etalon and should produce a beam shape flattened horizontally focused on the back of the VIPA etalon plate. The alignment of the cylindrical lens is also very long and sensitive and for that purpose a 3D translation stage on the VIPA or on the lens is needed. In addition the VIPA need the possibility to change the y-z inclination angle easily.

The third step regards checking if the alignment is enough accurate, and proceed to mount the grating. To check the alignment we can first check the power that should not be the same as before the etalon, and also check the shape of the beam after the etalon. The shape should resemble a vertical stripe blurred, otherwise the alignment is not performed in the right way. If the shape is correct we should aim for the maximum power after the etalon making sure that the shape is still a vertical stripe and is not changed. The power check can be a useful double-check, because is possible to follow a simple procedure:

Once this is done we can introduce the grating trying to aim the centre of the grating with the beam. After that we should mount and fix the CMOS camera at a distance from the grating that should be around 1.5 times the focal length of the spherical lens that will be introduced later. The camera should be fixed in the position when the beam is visible adjusting the height to have

Step	Meanings
Start: Power before=Power after	I am under the etalon
Move down the etalon	
Power drastically decrease	I am hitting the etalon but the reflection on the back plate is sending the beam out of the etalon
Move down the etalon	
Power increases, reaches a maximum and decreases	The beam is coupled inside the etalon
Try to position the etalon where the previous maximum is with small movements	
End: Find the maximum	

**Table 5.2.:** VIPA alignment step using power meter.

the beam centered.

The fourth step is introducing the spherical lens mounted on a 3D translation stage. The translation stage here is needed to focus on the camera with a fine tuning and have a clear image, and without any doubt this is the most difficult passage to complete. In fact to obtain a clear image focused all over the camera is necessary to check all the x-y-z direction of the translation stage multiple times. In the end the pattern achieved should resemble the one on the bottom right part of fig 5.6

# 6. Measurements, Results and Error Analysis

In this chapter are illustrated the measurements performed on the O<sub>2</sub> VIPA and the results obtained in order to reveal the O<sub>2</sub> absorption lines. The procedure followed for the measurements is briefly described here:

- Optimal alignment of the Frequency Comb (TOPTICA FemtoFERb 1560) and the CMOS camera (The Imaging Source DMK72BUC02)
- Localization of the FSR on the CMOS camera using a single mode diode laser (Roithner RLT7605MG)
- Installation of mass-flow controller (Bronkhorst EL-FLOW controller), pressure controller (Bronkhorst EL-FLOW controller) and vacuum pump (Pfeiffer DUO 10) to allow measurements of gas mixture inside the gas cavity
- Data acquisition and averaging with Labview C
- Data processing and analysis with MATLAB

## 6.1. Frequency Comb Alignment

The first step of the procedure is to align the Frequency Comb without the gas cavity on the optical path, achieve a focused image and then insert the gas cavity and optimizing the alignment. This part is particularly important and usually take a lot of time before the picture is perfectly focused on the CMOS camera.

The picture to aim for in this step is a picture with vertical narrow equidistant stripes, in addition the contrast of the stripes should be as high as possible to allow the software analysis, based on the localization of the stripes to process the data. In picture 6.1 is clear that the picture is not in focus at the bottom, while in picture 6.2 the focus of the image seems more uniform, although at the bottom the image is not focused like at the top.

The right settings for acquisition in this case are difficult to find considering the additional noise that is displayed on those two pictures. The vertical lines are present but is also possible to see a clear pattern of horizontal unexpected lines and some other dashed lines directed from the top right to bottom left of the image.

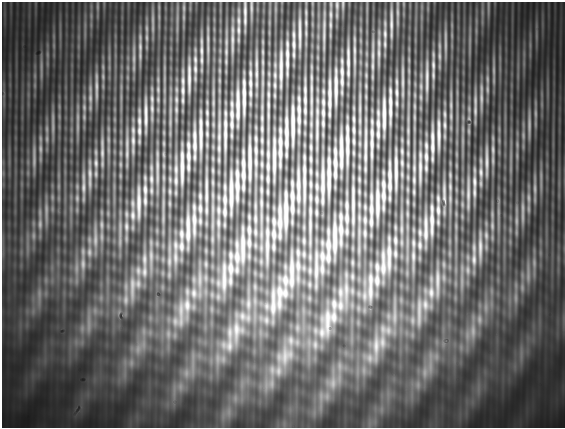


**Figure 6.1.:** Example of picture out of focus at the bottom

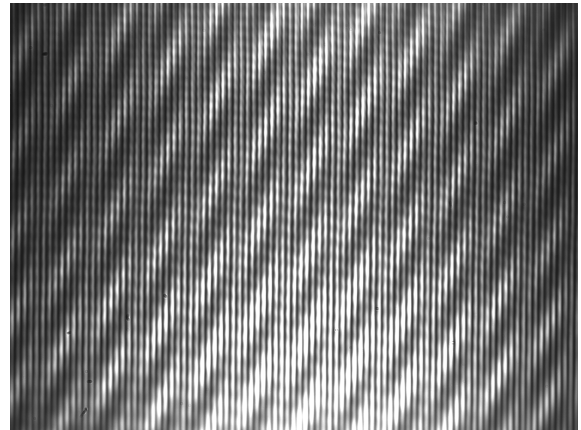


**Figure 6.2.:** This picture is more in focus but looking carefully at the bottom it is not in focus like at the top

To solve the problem and erase the noise all the alignment was checked several times, the spherical lens and the grating replaced with new components, but the noise pattern was still overlapped with the comb lines.

At this point was decided to proceed with the experiment and subtract the noise pattern with some software tools during the analysis project.

Anyway one hypothesis for this noise pattern is that the crystal operating the Second Harmonic Generation could have introduced some phase shift, making the beam lose the phase relation between the different wavelengths.

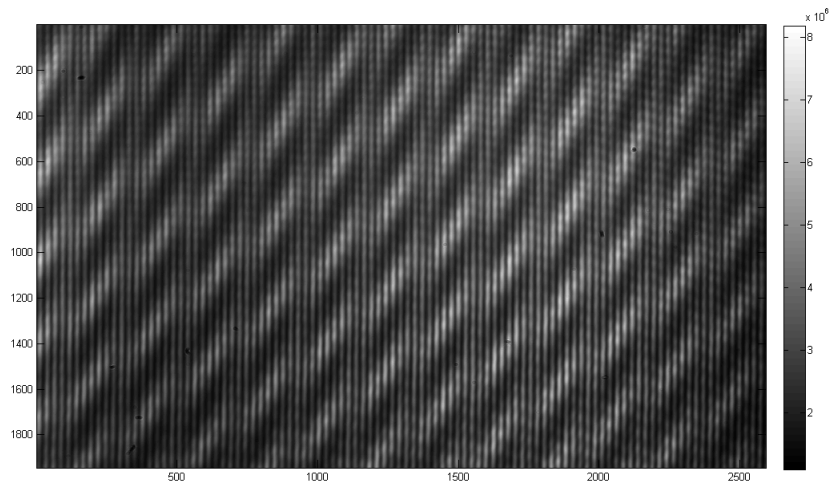


**Figure 6.3.:** Picture obtained with optimum settings and ambient air inside the cavity

At this point we tried to fix the optics elements in the optimal position to focus in a uniform way, than we set the gain and exposure time on the CMOS camera in order to have the higher contrast between the maxima and the minima (white lines, black lines) without modifying the minima

positions. Those settings were:

Gain = 6

Exposure time =  $0.01\bar{6}$  s

The picture obtained is showed in 6.3 and even if it seems darker than figure 6.2 the width of the lines is more uniform and less saturated and looking at the colorbar we can see that the difference between black and white is six order of magnitude, so we are confident is possible to process the data via software.

## 6.2. FSR localization on the CMOS camera

The second step after the comb alignment is the localization of the FSR on the CMOS camera. This step is important to know where to watch on the screen. In fact the pattern we should see is periodic pattern like the one obtained with the 1550 nm spectrometer 6.4. It is important to isolate only the area of the picture that is not periodic to have the correct data to process later.

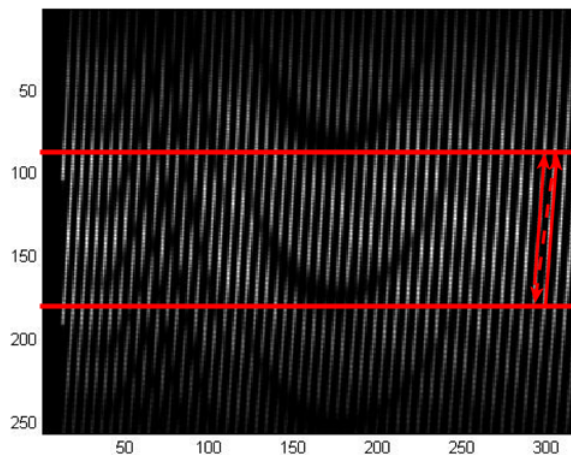


**Figure 6.4.:** Periodic pattern of CO<sub>2</sub> obtained with the 1550 nm spectrometer by Adonis Reyes Reyes [1]

In our case the comb measurements were noisy so we expect a picture that is not showing clear lines like 6.4 and to be sure to select the correct area we decide to use a reference laser.

The idea is to use a Continuous Wave (CW) single mode diode laser (Roithner RLT7605MG) with 757 nm wavelength, near to the Frequency Comb laser Second Harmonic. This laser should be collinear to the Frequency Comb and pass through the VIPA spectrometer.

The diode laser has a linewidth of 1 nm, so on the CMOS camera it should create a pattern of spots vertically aligned and equi-distant. In fact the VIPA spectrometer disperse the same

wavelength to different angles as explained in chapter 5 and between two spots of the same wavelength the whole FSR is present.

So just choosing the area between two spots we are sure we are covering the entire FSR, and we know we are watching in the region where the 757 nm are sent. In this sense when we send later the Frequency Comb into the VIPA spectrometer we already know which region of the picture to select and process numerically.

To do so a mirror was mounted on a translation stage to allow the diode laser to be collinear to the Frequency Comb, and to allow to keep the old alignment of the Frequency Comb ,when pulled back.

The first results were unexpected. We found that the lasing current intensity given by the manufacturer was not correct, so we increased the current to check if the lasing condition could be achieved or not. With higher currents the laser started lasing but the pattern we saw was not the one of a single mode diode laser with 1 nm linewidth.

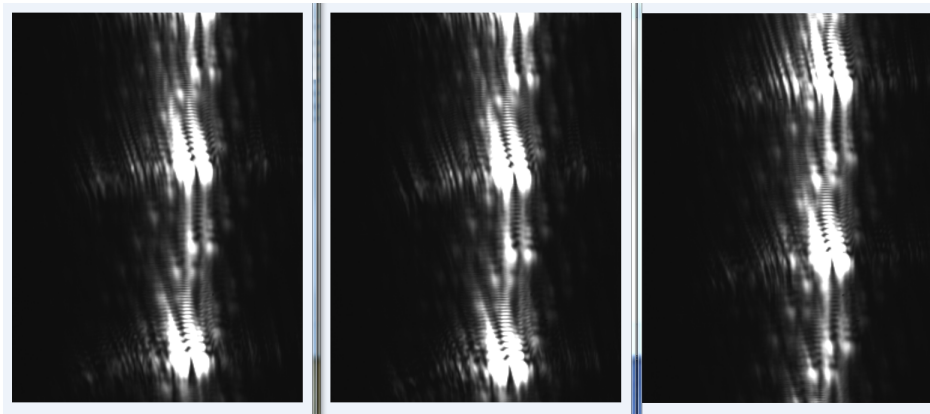


**Figure 6.5.:** Picture of the Reference diode laser with pump currents of 58 mA, 58.6 mA, 60.2 mA.

In picture 6.5 are illustrated three picture taken from the CMOS camera with current pump intensities of 58 mA, 58.6 mA, 60.2 mA. There are several unexpected features in this picture. First, the laser that was supposed to be single mode is showing a change of mode increasing the current from 58 mA to 60 mA. Second, the spot is not so clear and there are two spots aligned horizontally that are probably sign of some trouble on the laser source. Third, the picture shows that the laser linewidth could be also different from the one indicated by the manufacturer, because we do not see a clear spot.

To check the linewidth of the laser we use the Optical Spectrum Analyzer HP – 8562A and coupled the reference laser into it. The spectrum of the reference diode laser is showed in figure 6.6.

The current of the laser was set to 60.8 mA and the picture shows that the linewidth is more than 1 nm, on the order of 10nm. Precisely at the 3dB level it is 12.739 nm. With this linewidth the laser cannot produce the correct spots to give us the FSR localization.

For what regards the two horizontal unexpected spots we just check with a display card the beam shape before sending it into the VIPA spectrometer. As is possible to see in picture 6.7 the beam

has a hole in the middle and that is why we saw two horizontal spots on the camera.

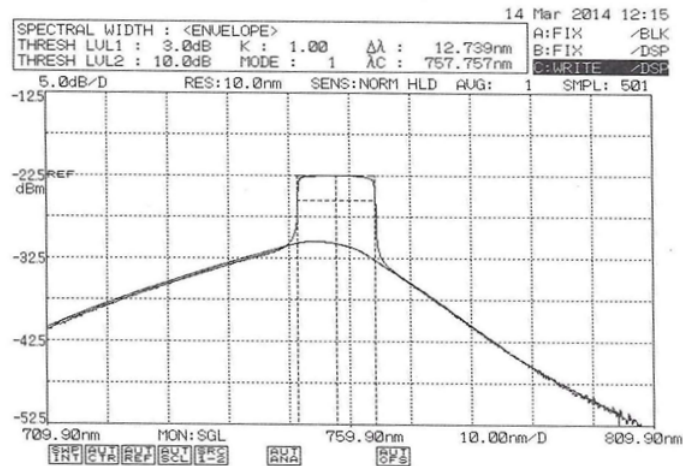


**Figure 6.6.:** Spectrum of the diode laser taken with a current intensity of 60.8 mA

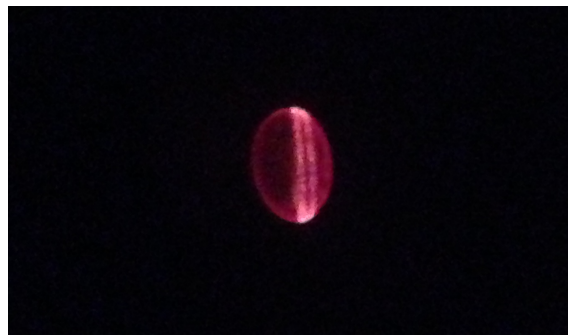


**Figure 6.7.:** Beam shape of the diode laser

The diode laser was replaced with a new functioning one and the spectrum of the new laser was checked again following the same coupling procedure.

The spectrum of the new diode laser is displayed in figure 6.8. Now the linewidth around the 3dB level is even lower than 1 nm, enough for accomplish our goal.

The FSR was successfully located and the area of interest is the one between the red lines in figure 6.9. Now the experiment can proceed and move to the next step.



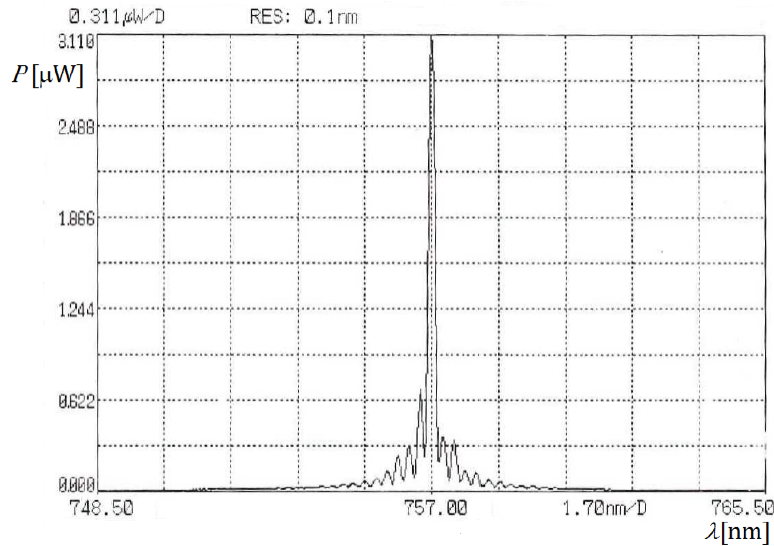


**Figure 6.8.:** Spectrum of the functioning reference diode laser

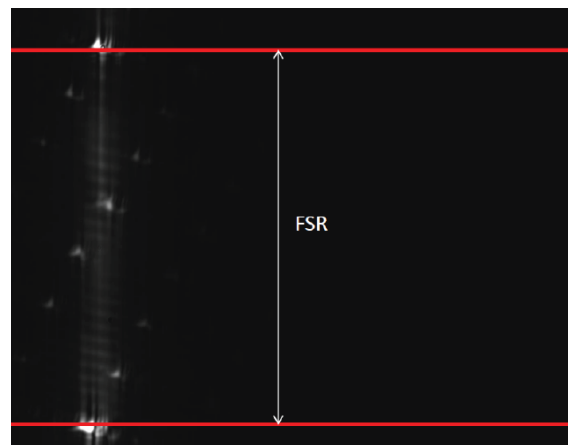


**Figure 6.9.:** FSR localization on the CMOS camera. The area of interest is between the red lines [6]

### 6.3. Data Acquisition

At this point we connect the gas cavity to the bottles of  $O_2$ ,  $CO_2$ ,  $N_2$  with the necessary pipes, together with a vacuum pump which was connected to the gas cavity. Three mass flow Bronkhorst EL-FLOW controllers were installed to control the gas flow and allow mixture of gas inside the cavity. A pressure controller Bronkhorst EL-FLOW is also present to control the pressure inside the cavity and evacuate when necessary.

In this way we are able to change gases inside the cavity, mix them, and change the pressure inside the cavity, all using a software interface. Using shutters we were also able to connect an external pipe that allow to inject ambient air inside the gas cavity.

After this is possible to proceed and acquire the data with a Labview program C. This program is averaging 25 images and saving a txt file.

The measurements plan is to acquire picture on the same conditions with the gas cavity full of  $N_2$ , evacuate the gas cavity, fill it again with  $O_2$  and operate the difference between them.

$N_2$  measurements will be regarded as reference measurements. More specifically the picture taken with  $N_2$  inside the gas cavity will be subtracted from the picture taken with  $O_2$  inside the gas cavity and the result will be processed.

After that a MATLAB program will analyze the pictures and extracts the  $O_2$  absorption lines. In picture 6.10 the difference between the picture taken with  $O_2$ , and the one taken with  $N_2$ , is displayed.

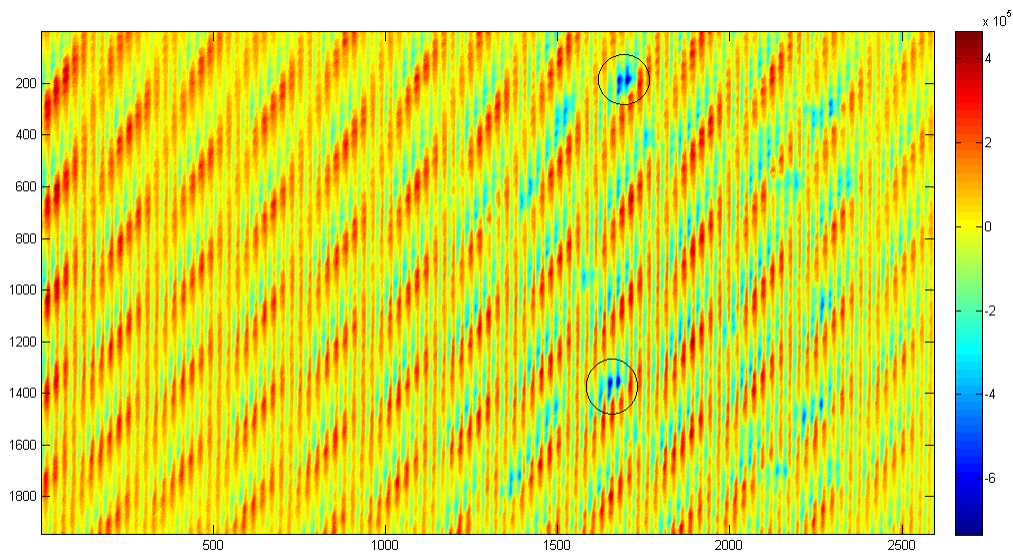


**Figure 6.10.:** Difference between the picture taken with  $O_2$ , and the one with  $N_2$ .

It is possible to see an artificial noise pattern that is affecting the measurement, and the difference in the measurements is not all due to absorption. Nevertheless there are some areas, surrounded in black, that are probably showing the wanted absorption. Adapting the MATLAB program to the VIPA spectrometer for  $O_2$  detection, we processed the picture but the result was not meaningful.

## 6.4. Noise sources

In order to find the noise sources long series of measurements were done. We took measurements in different conditions to be able later to process the data and find the noise sources.

The measurements were taken in different conditions, illustrated in table 6.4.

Kind of measurements	Expected Results	Real Results
10 serial picture, taken one every minute for N <sub>2</sub> and O <sub>2</sub>	Difference between 2 random O <sub>2</sub> , and two random N <sub>2</sub> near to zero	Expected
10 picture, evacuating the gas cavity between one pic and another, both for N <sub>2</sub> and O <sub>2</sub>	Difference between 2 random O <sub>2</sub> , and two random N <sub>2</sub> near to zero	The images suffer a shift
O <sub>2</sub> and N <sub>2</sub> pic taken with one hour delay one from the other	Difference between 2 random O <sub>2</sub> , and two random N <sub>2</sub> near to zero	Expected
Turn off the vacuum pump	Difference between measurements with pump on and pump off near to zero	Big difference between pics

**Table 6.1.:** Measurements done to find the noise sources

The possible ideas about the noise problems were connected to:

- Windows of the cavity not fixed, giving the shift
- Noise from the vibrations of the vacuum pump

To solve these noise problems, the windows of the gas cavity were replaced with fixed windows, and the measurements were taken with the vacuum pump turned off.

The picture achieved applying these solutions is showed in figure 6.11.

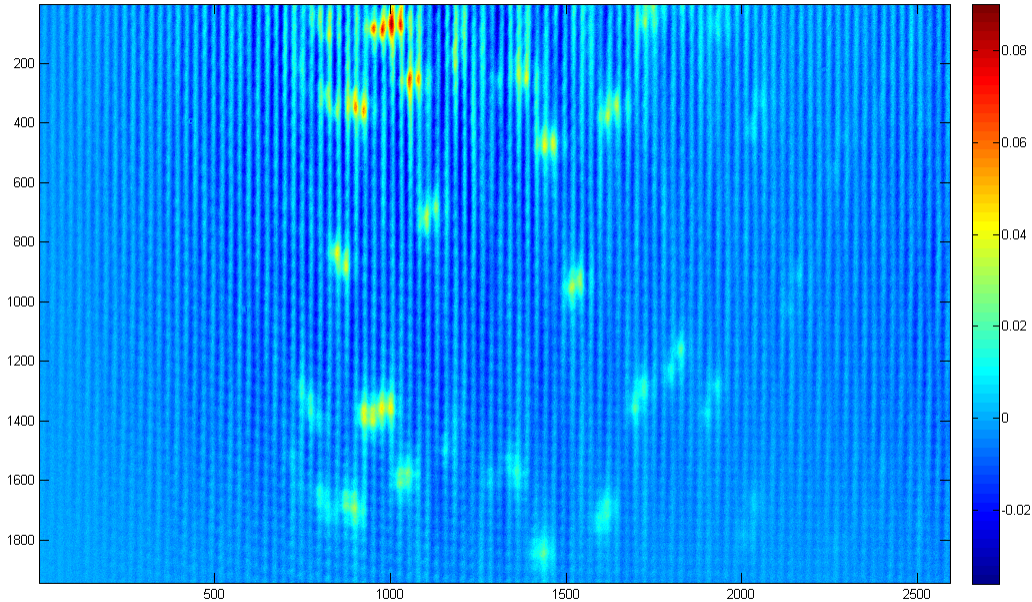


**Figure 6.11.:** Difference between O<sub>2</sub> picture and N<sub>2</sub> picture, after replacement of the gas cavity windows and with vacuum pump turned off [6].

The picture taken is the exact replica of figure 6.10, the only difference is that the vacuum pump now is turned off. In this picture the maximum difference is 0.087 compared to the  $10^5$  we had on picture 6.10. In addition the zones connected to absorption are visible even to bare eye without issues and there is a repeating pattern with the same size of the FSR in figure 6.9 . Now is possible to process the picture with the MATLAB program and to extract the  $O_2$  absorption lines.

The MATLAB program was developed by Adonis Reyes and has already been used to detect the absorption lines for  $CO_2$ , using the VIPA spectrometer and the original wavelength of the Frequency Comb. We just adapted the program for the  $O_2$  experiment changing the parameters that differ from the  $CO_2$  experiment.

The absorption spectrum given from the MATLAB program will be compared to the one stored on HITRAN online database for the same molecule and pressure (1 atm), in order to be fit and used for temperature measurements. The experimental and the HITRAN absorption spectra are displayed in figure 6.4.

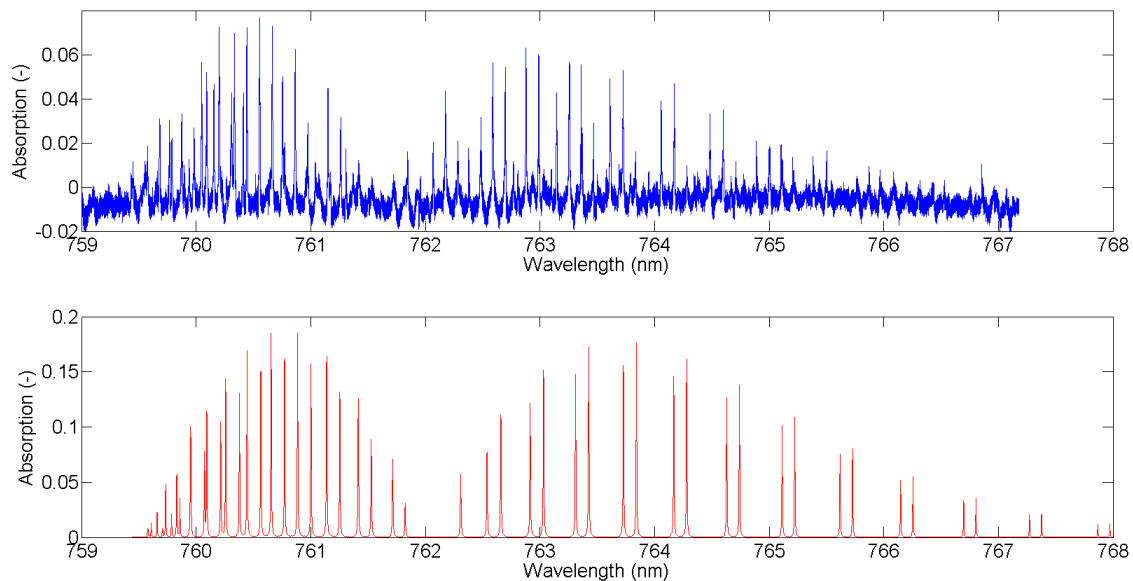


**Figure 6.12.:** The spectrum at the top is the spectrum obtained with the MATLAB program, the spectrum at the bottom is the spectrum taken by HITRAN database

The structure of the absorption profile shown in figure 6.4 is similar to the structure of the profile shown in the  $O_2$  spectrum from the HITRAN database. The two branches are due to vibrational transitions and the individual peaks inside each branches are due to rotational transitions in the molecule [6].

The MATLAB code still need to be optimised before proceeding to perform temperature measurements, because intensities and lines are not enough precise yet. Due to lack of time this part of the experiment were not completed.

Anyway a noise characterization was done and the standard deviation of the ratio of two reference camera images was calculated and found to be 0.024 and this introduces an intensity offset. This offset is due to the camera used to obtain the images.

In addition the signal to noise ratio (SNR) was calculated and the intensity contribution of the camera when the laser is turned off is  $7.8 \cdot 10^4$  and the maximum non saturated value when looking at the obtained measurement is  $14 \cdot 10^6$ .

For this specific measurement the SNR is estimated to be 45dB [6].

## 7. Conclusions and Discussion

The ultimate goal of the project is to perform temperature measurements via spectroscopy of two gases present in air, O<sub>2</sub> and CO<sub>2</sub>.

For CO<sub>2</sub> temperature measurements has already been done [1], while during the course of my thesis we built the O<sub>2</sub> VIPA spectrometer and aligned it. Measurements were achieved filling the gas cavity with O<sub>2</sub> and processing the pictures obtained using a MATLAB program to extract absorption spectra.

The results in chapter 6 needs to be optimised but are a good starting point.

The next step should be the improvement of the MATLAB code that converts the image into spectra, the increase of the SNR by changing camera settings and try improving the alignment of the VIPA spectrometer. The determination of the temperature via absorption spectra request the measurements spectrum to be matched with HITRAN spectrum to identify all the frequencies.

The final step will be to change the temperature of the cavity and obtaining absorption spectra at different temperatures.

# Bibliography

- [1] Adonis Reyes Reyes. Towards a trace gas detection setup using a viba spectrometer. Master's thesis, TU Delft, Delft, Netherlands, June 2009.
- [2] Ton Verhoeven. Temperature determination through spectroscopy. Master's thesis, TU Delft, 2014.
- [3] Andrew M. Weiner. *Ultrafast Optics*. Wiley, USA), 1st edition, 2009.
- [4] Steven R. Majewski. Astr 3130 lecture notes.
- [5] M. J. Thorpe. *Cavity-enhanced direct frequency comb spectroscopy*. PhD thesis, Faculty of the Graduate School, University of Colorado, 2009.
- [6] Remo van den Hoek. Temperature measurements using spectroscopy. Master's thesis, TU Delft, 2014.
- [7] T. Mayumi Wu Guanhao. Extremely high-accuracy correction of air refractive index using two-colour optical frequency combs. *Sci. Rep.*, 2013.
- [8] BENGT EDLÉN. The dispersion of standard air. *J. Opt. Soc. Am.*, 43(5):339–344, May 1953.
- [9] T. Hieta and M. Merimaa. Spectroscopic measurement of air temperature. *International Journal of Thermophysics*, 31(8-9):1710–1718, 2010.
- [10] Tuomas Hieta, Mikko Merimaa, Markku Vainio, Jeremias Seppä, and Antti Lassila. High-precision diode-laser-based temperature measurement for air refractive index compensation. *Appl. Opt.*, 50(31):5990–5998, Nov 2011.
- [11] D.J. Griffiths. *Introduction to Quantum Mechanics*. Pearson international edition. Pearson Prentice Hall, 2005.
- [12] S. T. Cundiff. Phase stabilization of ultrashort optical pulses. *J. Phys. D: Appl. Phys.*, 35:R43–R59, Apr 2002.
- [13] Robert W. Boyd. *Nonlinear Optics*. Acad. Press, 2003.
- [14] J. A. Armstrong, N. Bloembergen, J. Ducuing, and P. S. Pershan. Interactions between light waves in a nonlinear dielectric. *Phys. Rev.*, 127:1918–1939, Sep 1962.

- [15] M. Shirasaki. Virtually imaged phased array. *FUJITSU Sci.Tech.J.*, 1999.
- [16] M. Shirasaki. Large angular dispersion by a virtually imaged phased array and its application to a wavelength demultiplexer. *Opt. Lett.*, 21(5):366–368, Mar 1996.
- [17] Amnon Yariv. *Quantum electronics*. Wiley, 1989.
- [18] Shijun Xiao, A.M. Weiner, and C. Lin. A dispersion law for virtually imaged phased-array spectral dispersers based on paraxial wave theory. *Quantum Electronics, IEEE Journal of*, 40(4):420–426, April 2004.
- [19] M.V. Klein and T.E. Furtak. *Optics*. Wiley series in pure and applied optics. Wiley, 1986.
- [20] E. Hecht and A. Zajac. *Optics*. World student series. Addison-Wesley Pub. Co., 1974.



# Appendices

# A. Lambert-Beer law derivation

The Beer-Lambert law (or Beer's law) is the linear relationship between absorbance and concentration of an absorbing species. The general Beer-Lambert law is usually written as:

$$A = a(\lambda)bc \quad (\text{A.1})$$

where  $A$  is the measured absorbance,  $a(\lambda)$  is a wavelength-dependent absorptivity coefficient,  $b$  is the path length, and  $c$  is the analyte concentration. When working in concentration units of molarity, the Beer-Lambert law is written as:

$$A = \epsilon bc \quad (\text{A.2})$$

where  $\epsilon$  is the wavelength-dependent molar absorptivity coefficient with units of  $M^{-1}cm^{-1}$ .

## A.1. Derivation of Lambert-Beer law

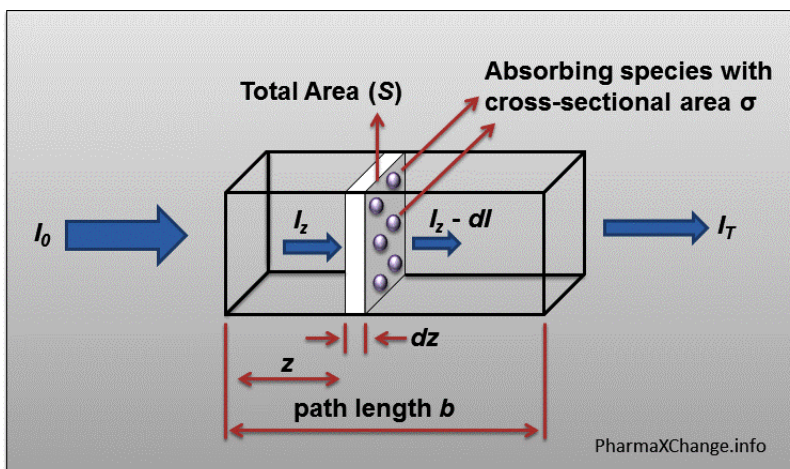
The Beer-Lambert law can be derived from an approximation for the absorption coefficient for a molecule by approximating the molecule by an opaque disk whose cross-sectional area,  $\sigma$ , represents the effective area seen by a photon of frequency  $\omega$ . If the frequency of the light is far from resonance, the area is approximately 0, and if  $\omega$  is close to resonance the area is a maximum. Taking an infinitesimal slab,  $dz$ , of sample:

$I_0$  is the intensity entering the sample at  $z = 0$ ,  $I_z$  is the intensity entering the infinitesimal slab at  $z$ ,  $dI$  is the intensity absorbed in the slab, and  $I$  is the intensity of light leaving the sample. Then, the total opaque area on the slab due to the absorbers is  $\sigma NSdz$ .

Then, the fraction of photons absorbed will be  $\frac{\sigma NSdz}{S}$  so,

$$\frac{dI}{I_z} = -\sigma Ndz \quad (\text{A.3})$$

Integrating this equation from  $z = 0$  to  $z = b$  gives:



$$\ln(I) - \ln(I_0) = -\sigma N b \quad (\text{A.4})$$

$$-\ln\left(\frac{I}{I_0}\right) = -\sigma N b \quad (\text{A.5})$$

Since

$$N \left( \frac{\text{molecules}}{\text{cm}^3} \right) \left( \frac{1 \text{ mole}}{6.023 \times 10^{23} \text{ molecules}} \right) \frac{1000 \text{ cm}^3}{\text{liter}} = c \left( \frac{\text{moles}}{\text{liter}} \right) \quad (\text{A.6})$$

then

$$-\ln\left(\frac{I}{I_0}\right) = \sigma (6.023 \times 10^{20}) c b \quad (\text{A.7})$$

$$-\ln\left(\frac{I}{I_0}\right) = A = \epsilon b c \quad (\text{A.8})$$

where  $\epsilon = \sigma (6.023 \times 10^{20})$

So we have the well known Lambert-Beer law

$$I = I_0 e^{-\epsilon c b} \quad (\text{A.9})$$

## B. Derivation of Parabolic equation for linear propagation

Starting from Maxwell equations

$$\nabla \cdot \mathbf{D} = \rho \quad (\text{B.1a})$$

$$\nabla \times \mathbf{E} = -\frac{\partial \mathbf{B}}{\partial t} \quad (\text{B.1b})$$

$$\nabla \cdot \mathbf{B} = 0 \quad (\text{B.1c})$$

$$\nabla \times \mathbf{B} = \mu_0 \left( J + \frac{\partial \mathbf{D}}{\partial t} \right) \quad (\text{B.1d})$$

where

$$\mathbf{D} = \epsilon_0 \mathbf{E} + \mathbf{P} \quad (\text{B.2})$$

$$\mathbf{B} = \mu_0 \mathbf{H} + \mathbf{M} \quad (\text{B.3})$$

In the case of interest  $\mathbf{M} = 0$  because the vector magnetization exists only in magnetic materials, and those material are not of interest in this case. In addition we consider the material as free from free charges and currents so  $\rho = 0, J = 0$ . The equations are now:

$$\nabla \cdot \mathbf{D} = 0 \quad (\text{B.4a})$$

$$\nabla \times \mathbf{E} = -\frac{\partial \mathbf{B}}{\partial t} \quad (\text{B.4b})$$

$$\nabla \cdot \mathbf{B} = 0 \quad (\text{B.4c})$$

$$\nabla \times \mathbf{B} = \mu_0 \frac{\partial \mathbf{D}}{\partial t} \quad (\text{B.4d})$$

Now using a property of the rotor  $\nabla \times \nabla \times \mathbf{E} = \nabla(\nabla \cdot \mathbf{E}) - \nabla^2 \mathbf{E}$  and equation B.4b

$$\nabla \times \nabla \times \mathbf{E} = \nabla \times \left( -\frac{\partial \mathbf{B}}{\partial t} \right) = -\frac{\partial}{\partial t} (\nabla \times \mathbf{B}) = -\frac{\partial}{\partial t} \left( \mu_0 \frac{\partial \mathbf{D}}{\partial t} \right) \quad (\text{B.5})$$

$$= -\mu_0 \frac{\partial^2 \mathbf{B}}{\partial t^2} \quad (\text{B.6})$$

For a general vector  $\nabla(\nabla \cdot \mathbf{E}) = 0$  so

$$\nabla^2 \mathbf{E} = \mu_0 \frac{\partial^2 \mathbf{B}}{\partial t^2} \quad (\text{B.7})$$

Using equation B.2

$$\nabla^2 \mathbf{E} = \mu_0 \frac{\partial^2}{\partial t^2} (\epsilon_0 \mathbf{E} + \mathbf{P}) \quad (\text{B.8})$$

It is possible now to introduce the scalar approximation  $\nabla^2 = \frac{\partial^2}{\partial z^2}$ , and the plane wave approximation  $E = E(z)$ , where  $z$  is the wave propagation direction and the electric field does not depend on transverse coordinates. The equation is reduced to:

$$\frac{\partial^2 E(z,t)}{\partial z^2} - \frac{1}{c^2} \frac{\partial^2 E(z,t)}{\partial t^2} = \mu_0 \frac{\partial^2 P(z,t)}{\partial t^2} \quad (\text{B.9})$$

Considering a pulse, the electric field can be written as product of an envelope and a carrier:

$$E(z,t) = \text{Re} \left\{ A(z,t) e^{i(\omega_0 t - k_0 z)} \right\} \quad (\text{B.10})$$

The polarization is :

$$P = P_L + P_{NL} \quad (\text{B.11})$$

For now we only consider the linear polarization  $P_L$  that is :

$$P(z,t) = e^{i(\omega_0 t - k_p z)} \quad (\text{B.12})$$

Now the idea is to use the Fourier Transform to simplify the equation in this way:

$$\mathcal{F} \left\{ \frac{\partial^2 E(z,t)}{\partial z^2} \right\} - \mathcal{F} \left\{ \frac{1}{c^2} \frac{\partial^2 E(z,t)}{\partial t^2} \right\} = \mathcal{F} \left\{ \mu_0 \frac{\partial^2 P(z,t)}{\partial t^2} \right\} \quad (\text{B.13})$$

$$\frac{\partial^2 \tilde{E}}{\partial z^2} - (i\omega)^2 \tilde{E} = \mu_0 (i\omega)^2 \tilde{P} \quad (\text{B.14})$$

where  $\tilde{E}$  is the fourier transform of the original  $E(z,t)$ :

$$\tilde{E}(z, \omega) = \int_{-\infty}^{\infty} A(z,t) e^{i(\omega_0 t - k_0 z)} e^{-i\omega t} dt \quad (\text{B.15})$$

$$= \int_{-\infty}^{\infty} A(z,t) e^{-ik_0 z} e^{-i(\omega - \omega_0)t} dt \quad (\text{B.16})$$

$$= e^{-ik_0 z} \int_{-\infty}^{\infty} A(z,t) e^{-i(\omega - \omega_0)t} dt \quad (\text{B.17})$$

$$= \tilde{A}(z, \omega - \omega_0) e^{-ik_0 z} \quad (\text{B.18})$$

At this point we calculate the first and second derivative of  $\tilde{E}$  (hiding the dependence from  $(\omega - \omega_0, z)$  to simplify the notation):

$$\frac{\partial \tilde{E}}{\partial z} = -ik_0 e^{ik_0 z} \tilde{A} + e^{ik_0 z} \frac{\partial \tilde{A}}{\partial z} \quad (\text{B.19})$$

$$\frac{\partial^2 \tilde{E}}{\partial z^2} = -k_0^2 e^{ik_0 z} \tilde{A} - 2ik_0 e^{ik_0 z} \frac{\partial \tilde{A}}{\partial z} + e^{ik_0 z} \frac{\partial^2 \tilde{A}}{\partial z^2} \quad (\text{B.20})$$

Using the Slowly Varying Amplitude Approximation (SVEA) we can drop the second derivative term because

$$\frac{\partial^2 \tilde{A}}{\partial z^2} \ll 2ik_0 \frac{\partial \tilde{A}}{\partial z} \quad \text{in other words} \quad (\text{B.21})$$

$$2i \frac{2\pi}{\lambda_0} \frac{\partial \tilde{A}}{\partial z} \gg \frac{\partial}{\partial z} \left( \frac{\partial \tilde{A}}{\partial z} \right) \quad (\text{B.22})$$

because  $\tilde{A}$  is considered as slowly varying for a propagation  $\approx \lambda_0$ . So the second derivative of the electric field transform is

$$\frac{\partial^2 \tilde{E}}{\partial z^2} = -k_0^2 e^{ik_0 z} \tilde{A} - 2ik_0 e^{ik_0 z} \frac{\partial \tilde{A}}{\partial z} \quad (\text{B.23})$$

The Fourier transform of the polarization term is treated like the electric field and it is:

$$\tilde{P}(z, \omega) = e^{ik_0 z} \tilde{p}(z, \omega - \omega_0) \quad (\text{B.24})$$

The equation B.14 now become:

$$-k_0^2 e^{ik_0 z} \tilde{A} - 2ik_0 e^{ik_0 z} \frac{\partial \tilde{A}}{\partial z} + \frac{\omega^2}{c^2} \tilde{A} e^{ik_0 z} = \mu_0 \omega^2 \tilde{P}(z, \omega - \omega_0) \quad (\text{B.25})$$

writing  $\tilde{p}(z, \omega - \omega_0)$  remembering that (the dependence on  $\omega - \omega_0$  remains, we use only  $\omega$  to simplify the notation):

$$\tilde{P}(\omega) = \varepsilon_0 \chi(\omega) \tilde{E}(\omega) \quad \text{we have} \quad (\text{B.26})$$

$$\tilde{p}(\omega) = \varepsilon_0 \chi(\omega) \tilde{A} \quad (\text{B.27})$$

$$n(\omega)^2 = 1 + \chi(\omega) \quad \text{that insert in the previous gives} \quad (\text{B.28})$$

$$\tilde{p}(\omega) = \varepsilon_0 [n(\omega)^2 - 1] \tilde{A} \quad (\text{B.29})$$

Inserting B.28 B.29 in equation B.25:

$$+k_0^2 \tilde{A} + 2ik_0 \frac{\partial \tilde{A}}{\partial z} - \frac{\omega^2}{c^2} \tilde{A} = \omega^2 \mu_0 \varepsilon_0 [n(\omega)^2 - 1] \tilde{A} = \frac{\omega^2}{c^2} [n(\omega)^2 - 1] \tilde{A} \quad (\text{B.30})$$

Moving the term with  $\tilde{A}$  to the right hand side of the equation and rewriting it we have

$$2ik_0 \frac{\partial \tilde{A}}{\partial z} = \tilde{A} \left[ \frac{\omega^2}{c^2} n(\omega) - k_0^2 \right] \quad (\text{B.31})$$

Now the term inside square brackets can be written as  $[k(\omega)^2 - k_0^2]$  because  $k(\omega)^2 = \frac{\omega^2}{c^2} n(\omega)$  and can be unwrapped in this way:

$$[k(\omega)^2 - k_0^2] = [k(\omega) + k_0][k(\omega) - k_0] \approx 2k_0[k(\omega) - k_0] \quad (\text{B.32})$$

because  $\omega \approx \omega_0$ . Expanding  $k(\omega - \omega_0)$  with Taylor :

$$k(\omega) = k(\omega_0) + \left. \frac{\partial k}{\partial \omega} \right|_{\omega_0} (\omega - \omega_0) + \frac{1}{2} \left. \frac{\partial^2 k}{\partial \omega^2} \right|_{\omega_0} (\omega - \omega_0)^2 + \frac{1}{6} \left. \frac{\partial^3 k}{\partial \omega^3} \right|_{\omega_0} (\omega - \omega_0)^3 + \dots \quad (\text{B.33})$$

The terms in the previous equation are physically important, because:

$$k(\omega_0) = k_0 \quad \text{for definition} \quad (\text{B.34a})$$

$$\left. \frac{\partial k}{\partial \omega} \right|_{\omega_0} = k'_0 = \frac{1}{v_{g0}} \quad \text{inverse of group velocity} \quad (\text{B.34b})$$

$$\left. \frac{\partial^2 k}{\partial \omega^2} \right|_{\omega_0} = k''_0 = GVD \quad \text{group velocity dispersion} \quad (\text{B.34c})$$

$$\left. \frac{\partial^3 k}{\partial \omega^3} \right|_{\omega_0} = k'''_0 \quad \text{can be left out because not influent} \quad (\text{B.34d})$$

Equation B.31 now is:

$$i \frac{\partial \tilde{A}}{\partial z}(\omega - \omega_0, z) = \frac{1}{v_{g0}}(\omega - \omega_0)\tilde{A} + \frac{GVD}{2}(\omega - \omega_0)^2\tilde{A} \quad (\text{B.35})$$

where we displayed again the dependence from  $\omega - \omega_0$  and  $z$ .

If we transform back we obtain

$$i \frac{\partial A}{\partial z}(t, z) = \frac{1}{v_{g0}}(-i) \frac{\partial A}{\partial t} + (-i^2) \frac{GVD}{2} \frac{\partial^2 A}{\partial t^2} \quad (\text{B.36})$$

$$\frac{\partial A}{\partial z}(t, z) + \frac{1}{v_{g0}} \frac{\partial A}{\partial t} - GVD \frac{i}{2} \frac{\partial^2 A}{\partial t^2} = 0 \quad (\text{B.37})$$

This is the parabolic equation for linear propagation for the envelope  $A(t, z)$ . In the case of nonlinear polarization at the right hand side of the equation we will have a term that contains the nonlinearity.



## C. Labview Program

The following labview program was used to acquire and average 25 snapshot from the CMOS camera, and give in output a 60 MB text file to process with Matlab.

The pictures are acquired one by one in a format RGB  $2592 \times 1944$  pixels, converted in a 32 bit levels matrix , added with the previous image. The final added matrix is divided by the number of images giving a 64 bit levels matrix text file.

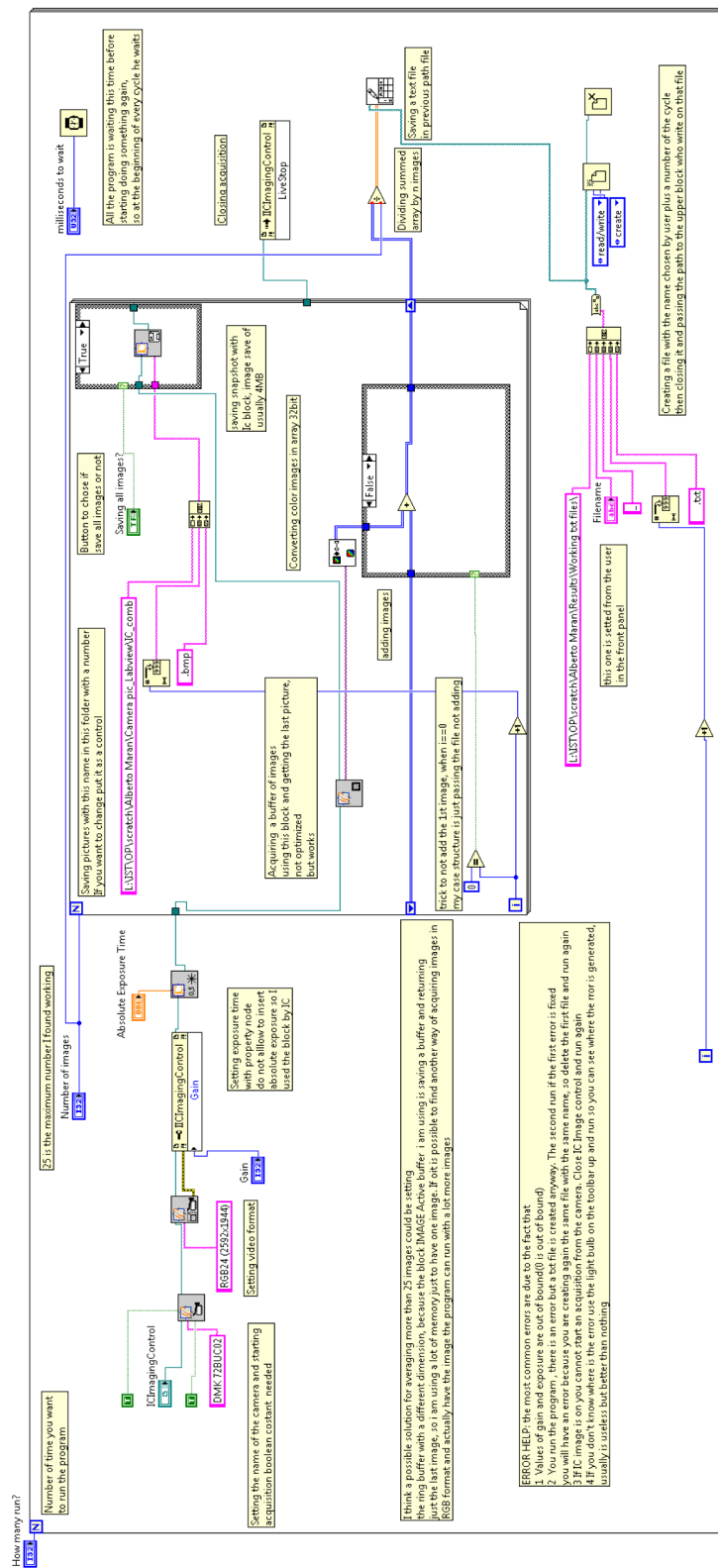


Figure C.1.: Labview program for acquisition and averaging of 25 pictures.